2009

DUST-CORRECTED STAR FORMATION RATES OF GALAXIES. I. COMBINATIONS OF H alpha AND INFRARED TRACERS

RC Kennicutt

CN Hao

D Calzetti

J Moustakas

DA Dale

See next page for additional authors

Recommended Citation

Kennicutt, RC; Hao, CN; Calzetti, D; Moustakas, J; Dale, DA; Bendo, G; Engelbracht, CW; Johnson, BD; and Lee, JC, "DUST-CORRECTED STAR FORMATION RATES OF GALAXIES. I. COMBINATIONS OF H alpha AND INFRARED TRACERS" (2009). *ASTROPHYSICAL JOURNAL*. 134.
10.1088/0004-637X/703/2/1672

Dust-Corrected Star Formation Rates of Galaxies. I. Combinations of Hα and Infrared Tracers

Robert C. Kennicutt, Jr.[1,2], Cai-Na Hao[1], Daniela Calzetti[3], John Moustakas[4,5], Daniel A. Dale[6], George Bendo[7], Charles W. Engelbracht[2], Benjamin D. Johnson[1], and Janice C. Lee[8]

ABSTRACT

We combine Hα emission-line and infrared continuum measurements of two samples of nearby galaxies to derive dust attenuation-corrected star formation rates (SFRs). We use a simple energy balance based method that has been applied previously to HII regions in the Spitzer Infrared Nearby Galaxies Survey (SINGS), and extend the methodology to integrated measurements of galaxies. We find that our composite Hα + IR based SFRs are in excellent agreement with attenuation-corrected SFRs derived from integrated spectrophotometry, over the full range of SFRs (0.01 – 80 $M_\odot\,yr^{-1}$) and attenuations (0 – 2.5 mag) studied. We find that the combination of Hα and total infrared luminosities provides the most robust SFR measurements, but combinations of Hα measurements with monochromatic luminosities at 24 μm and 8 μm perform nearly as well. The calibrations differ significantly from those obtained for HII regions (Calzetti et al. 2007), with the difference attributable to a more evolved population of stars heating the dust. Our results are consistent with a significant component of diffuse dust (the 'IR cirrus' component) that is heated by a non-star-forming

[1]Institute of Astronomy, University of Cambridge, Madingley Road, Cambridge CB3 0HA, UK

[2]Steward Observatory, University of Arizona, Tucson, AZ 85721, USA

[3]Department of Astronomy, University of Massachusetts, Amherst, MA 01003, USA

[4]Center for Astrophysics and Space Sciences, University of California, San Diego, 9500 Gilman Drive, La Jolla, California, 92093, USA

[5]Center for Cosmology and Particle Physics, New York University, 4 Washington Place, New York, NY 10003, USA

[6]Department of Physics, University of Wyoming, Laramie, WY 82071, USA

[7]Blackett Laboratory, Imperial College London, Prince Consort Road London, England SW7 2AZ, UK

[8]Carnegie Observatories, 813 Santa Barbara Street, Pasadena, CA 91101, USA

population. The same methodology can be applied to [O II]λ3727 emission-line measurements, and the radio continuum fluxes of galaxies can be applied in place of IR fluxes when the latter are not available. We assess the precision and systematic reliability of all of these composite methods.

Subject headings: dust, attenuation; galaxies: ISM — galaxies: evolution — HII regions — stars: formation

1. INTRODUCTION

Interstellar dust absorbs and reprocesses approximately half of the starlight in the Universe (Lagache et al. 2005), and this extinction introduces the largest source of systematic error into measurements of star formation rates (SFRs) in galaxies (Kennicutt 1998a, hereafter denoted as K98, and references therein). In present-day disk galaxies the typical dust attenuations[1] are of order 0–2 mag in Hα and 0–4 mag in the non-ionizing ultraviolet continuum ($\sim 130 - 250$ nm), the most commonly used SFR tracers (e.g., Kennicutt 1983; Brinchmann et al. 2004; Buat et al. 2005). The resulting systematic error in the overall SFR scales can be largely removed by applying a statistical correction for the dust attenuation (e.g., Kennicutt 1983; Calzetti et al. 1994, 2000). However the attenuation within and between individual galaxies varies from virtually zero to several magnitudes (K98 and references above), so even if the systematic effect is removed SFRs for individual galaxies will suffer typical random errors of a factor of two or more. Emission-line diagnostics such as the Balmer decrement or the Pa α/Hα ratio correct the Hα SFR measurements for attenuation (e.g., Kewley et al. 2002; Brinchmann et al. 2004; Moustakas et al. 2006), but such spatially-resolved spectrophotometry is difficult to obtain and not widely available. Likewise at ultraviolet (UV) wavelengths the slope of the continuum can be used to estimate an attenuation correction, but the large scatter in the attenuation vs UV color relation makes such corrections highly uncertain (e.g., Meurer et al. 1999; Kong et al. 2004; Dale et al. 2007; Johnson et al. 2007a; Cortese et al. 2008).

An alternative approach to estimating the SFR in very dusty galaxies is to measure one or more components of the mid- and far-infrared emission. In the limit of complete

[1]We adopt the convention of using the term extinction to describe the combined effect of scattering and absorption of starlight by intervening dust grains, and the term attenuation to describe the net reduction of starlight in an extended source such as a galaxy, in which stars and dust are mixed in a complex geometry. Attenuation includes the effects of differential embedding of stars within the dust distribution as well as absorption of starlight by dust, with part of the scattered radiation being returned to the observer.

obscuration the dust will re-emit the bolometric luminosity of the embedded stars, and if young stars produce most of the integrated starlight the re-emitted infrared (IR) luminosity will effectively provide a bolometric measure of the SFR (K98). This combination of a high dust optical depth and a young star dominated radiation field is often satisfied in the most actively star-forming galaxies in the Universe, the luminous infrared (LIRG) and ultraluminous infrared galaxies (ULIRGs). Consequently most of our knowledge of the star-formation properties of IR-luminous starburst galaxies comes from measurements of the IR dust continuum emission. Although the total integrated IR emission of galaxies should provide the most robust measure of the dust-enshrouded SFR, calibrations based at specific wavebands such as the rest $8\,\mu$m and $24\,\mu$m emission have been derived by various authors (e.g., Calzetti et al. 2005,2007; Wu et al. 2005; Alonso-Herrero et al. 2006; Pérez-González et al. 2006; Relaño et al. 2007; Bavouzet et al. 2008; Zhu et al. 2008; Rieke et al. 2009).

Although the dust emission by itself can provide a reliable measure of the SFR in the most obscured circumnuclear starbursts, its application as a quantitative SFR tracer in normal galaxies suffers from its own set of systematic errors. Since the typical attenuation of young starlight in normal galaxies is only of order 1 mag, this implies that roughly half of the starlight is *not* processed by dust, and this in turn will tend to cause the IR emission to systematically under-estimate the SFR. The problem is much more severe in gas- or metal-poor environments such as dwarf galaxies and the outer disks of galaxies, where the fraction of obscured star formation can become negligible (e.g., Wang & Heckman 1996; Bell 2003). Another, competing systematic effect is the contribution to dust heating by more evolved stars, sometimes referred to as the "infrared cirrus" problem (K98 and references therein). The effects of finite dust opacity and cirrus contamination tend to be of roughly comparable magnitude in typical massive star-forming spiral galaxies, and thanks to this coincidence the SFRs derived from IR measures are often surprisingly consistent with those derived from other methods (e.g., Sauvage & Thuan 1992; Kewley et al. 2002). However this coincidence breaks down in other types of galaxies.

Since the starlight removed at short wavelengths by the interstellar dust is re-radiated in the IR, it should be possible to calibrate a much more robust set of attenuation-corrected star formation tracers by combining observations in the UV or visible with those in the infrared. In recent years this approach has been applied widely using the combination of UV and IR observations to estimate dust-corrected SFRs (e.g., Gordon et al. 2000; Bell 2003; Hirashita et al. 2003; Iglesias-Páramo et al. 2006; Cortese et al. 2008), and has been explored for Hα and IR-based SFR measurements by Inoue (2001), Inoue et al. (2001), and Hirashita et al. (2001, 2003). However the absence of an independent set of attenuation-corrected SFRs has made it difficult to assess the reliability of these corrected SFRs, and to calibrate the relation between effective UV attenuation and the ratio of IR to UV luminosities.

The advent of large sets of multi-wavelength observations of nearby galaxies now provides us with the opportunity to derive attenuation-corrected Hα and UV continuum luminosities of galaxies by combining these fluxes with various components of the IR emission. Moreover the availability of integrated optical spectra (and in some cases Pa α maps) of the same galaxies allows us to derive additional attenuation estimates, and test the precision and systematic reliability of the respective attenuation-corrected SFR measurements.

The Spitzer Infrared Nearby Galaxies Survey (SINGS; Kennicutt et al. 2003) offers an ideal dataset for testing and calibrating such multi-wavelength SFR estimators. The survey includes imaging of a diverse sample of 75 galaxies within 30 Mpc, with wavelength coverage extending from the UV to the radio, including ultraviolet imaging at 150 and 230 nm, Hα, and 7 infrared wavelengths over 3.6 – 160 μm. In addition, drift-scanned spectra over the wavelength range 3600 – 6900 Å are available, which complement matching infrared spectra over the range 10 – 40 μm. We first applied these data to calibrate and test the combined use of Hα and 24 μm infrared fluxes of individual HII regions to derive attenuation-corrected emission-line fluxes (Calzetti et al. 2007, hereafter denoted C07; Kennicutt et al. 2007; Prescott et al. 2007). These studies revealed that the Spitzer 24 μm sources were highly correlated in position and flux with those of optical HII region counterparts. Kennicutt et al. (2007) and C07 found that the ratio of 24 μm to Hα fluxes yielded attenuation-corrected Hα luminosities and attenuation values that were consistent with those derived from Paα/Hα reddening measurements, extending over ranges of >3 mag in A(Hα) and more than 4 orders of magnitude in ionizing luminosity and Hα surface brightness, albeit with a large random error (approximately $\pm$0.3 dex) that probably arises from variations in stellar population and dust geometry, as discussed later.

In this paper we now explore whether the same approach of combining Hα and IR observations can be used to derive reliable attenuation-corrected SFRs of entire galaxies. Our analysis combines SINGS observations with integrated spectra and IR observations of a larger sample of galaxies from Moustakas & Kennicutt (2006). We find that excellent estimates of attenuation-corrected SFRs can be derived by combining Hα emission-line luminosities with 24μm, total infrared (TIR), and even 8μm IR luminosities. We provide prescriptions for each of these multi-wavelength SFR tracers, and also test other combinations of tracers, including combinations of [O II]λ3727 and IR luminosities, and combinations of emission-line and radio continuum luminosities. A companion paper (Hao et al. 2009, hereafter denoted Paper II) uses the same galaxies to empirically calibrate the combination of UV and IR luminosities to measure attenuation-corrected SFRs.

The remainder of this paper is organized as follows. In §2 we describe the multi-wavelength dataset that was compiled for this analysis. In §3 we describe our method for

combining Hα and IR fluxes of galaxies to estimate the Hα attenuation, and discuss the assumptions and limitations that underlie the method. In §4 we use the integrated 24 μm, TIR, and Hα fluxes of the galaxies in our sample to calibrate the method, and test for systematic dependencies of the results on the spectral energy distributions (SEDs), star formation properties, and physical properties of the galaxies. In §5 we extend the approach to other composite SFR indicators, including combinations of optical emission lines with 8 μm (PAH-dominated) IR luminosities and radio continuum luminosities. In §6 we use the results to re-examine the systematic reliability of the methods. We summarize our results in §7.

2. DATA

2.1. Galaxy Sample

Our basic approach is to compare and calibrate global attenuation estimates for galaxies derived from the combination of Hα and IR luminosities of galaxies with independently derived attenuation measures from integrated optical emission-line spectra. Our samples are drawn from two surveys of nearby galaxies, the SINGS survey (Kennicutt et al. 2003) and a survey of integrated spectrophotometry of 417 galaxies by Moustakas & Kennicutt (2006; hereafter denoted MK06).[2] The SINGS sample is comprised of 75 galaxies with distances less than 30 Mpc, which were chosen to span wide ranges in morphological type, luminosity, and dust opacity. The MK06 survey was designed to include the full range of optical spectral characteristics found in present-day galaxies, and includes a subsample of normal galaxies as well as large subsamples of optically-selected starburst galaxies and infrared-luminous galaxies. The combined sample includes objects ranging from dwarf irregular galaxies to giant spirals and IR-luminous galaxies ($-13.4 \geq M_B \geq -22.4$), with SFRs of $\sim$0.001 – 100 $M_\odot\,yr^{-1}$, and $\sim 0.01 < L_{IR}/L_B < 100$. This diversity is important for testing the applicability limits for our methods, and for uncovering any second-order dependences of our results on properties of the galaxies or their SEDs. Detailed information about the SINGS and MK06 samples can be found in the respective survey papers.

Our analysis draws on subsets of these samples which satisfy a number of further selection criteria. Galaxies showing no detectable star formation as measured at Hα were excluded; most of those were early-type E and S0 galaxies. Likewise we required that the

[2]During the early phases of our study our sample also included the Nearby Field Galaxy Survey (Jansen et al. 2000). However after the sample was vetted for minimum signal/noise and matching IR data only a handful of galaxies remained. As a result we chose to restrict our analysis to the SINGS and MK06 samples.

galaxies had well-measured infrared fluxes or strong upper limit fluxes from *Spitzer* (SINGS sample) and/or *IRAS* (for both samples), as discussed further in §2.4. We also applied a signal/noise requirement on the optical spectra, to ensure an accurate measurement of the Balmer decrement (Hα/Hβ ratio). This was done by a combination of formal signal/noise estimates and visual inspection of the continuum-subtracted spectra at Hβ. This translated to a minimum $S/N \sim 15$ at Hβ. Finally, we separated galaxies with spectra dominated by star formation from those with bright active galactic nuclei (AGN-dominated) or composites of star formation and AGN signatures, so their behavior could be analyzed separately. This separation was performed using the optical emission-line spectra, using the criteria of Kewley et al. (2001) and Kauffmann et al. (2003) criteria as described in Moustakas et al. (2006).

Application of these minimum signal/noise criteria in IR photometry, Hα photometry, and spectroscopic S/N yielded subsamples of 58 SINGS galaxies (including 4 AGN-dominated galaxies, NGC 3190, NGC 4550, NGC 4569, and NGC 4579), and 147 galaxies from MK06 (including 3 AGN-dominated galaxies and 31 with composite nuclei). The galaxy population retains the mixture of the parent samples, with normal spiral and irregular galaxies and especially strong representation of UV, blue, and IR-selected starburst galaxies.

This combination of selection criteria (adequate signal/noise in the infrared continuum and Balmer emission lines, emission-line spectra dominated by star formation) was applied to provide an accurate calibration of the attenuation-correction methods that are developed in this paper. However it is important to bear in mind that these criteria tend to favor the selection of galaxies with significant SFRs per unit mass, typically intermediate to late-type spiral galaxies and luminous irregular and starburst galaxies. Objects that tend to be excluded include early-type (E, S0, Sa) galaxies with weak line emission, dwarf irregular galaxies with little or no detectable dust emission, and the most highly obscured infrared luminous and ultraluminous galaxies, which tend to exhibit weak Hβ line emission and (frequently) AGN signatures in their spectra. Some of these selection effects are unimportant, for example the absence of IR-weak galaxies from the sample is irrelevant because no attenuation correction is required in those cases. However the very early-type galaxies and extreme starbursts may probe star formation and attenuation regimes that fall outside of the valid range of our calibrations. We discuss the potential effects of these selection effects further in §6.

2.2. Optical Emission-Line Spectra and Balmer Decrements

Integrated Hα fluxes and Hα/Hβ flux ratios for the MK06 sample were taken directly from the integrated spectra. The galaxies were observed with the B&C Spectrograph on the Steward Observatory Bok 2.3 m telescope using a long-slit drift-scanning technique, which produced an integrated spectrum over a rectangular aperture that covered most or all of each galaxy. The resolution of the spectra ($\sim$8 Å) is sufficient to deblend Hα from the neighboring [NII]$\lambda\lambda$6548,6584 lines. The underlying continuum and absorption-line spectra were fitted and removed as part of the emission-line flux measurements, which removes the effects of stellar Balmer absorption on the Hα and Hβ measurements (see MK06 for details).

Drift-scanned spectra were also obtained for the SINGS sample, using the same instrument and setup as MK06 for northern galaxies, and the R-C spectrograph on the CTIO 1.5 m telescope for a handful of galaxies that could not be reached from Kitt Peak. These observations were configured to match the spatial coverage of the mid-IR spectral maps obtained as part of SINGS. Mapping entire galaxies was not practical with the *Spitzer* Infrared Spectrograph (IRS), so we mapped representative sub-regions of the galaxies instead. One set of optical observations consisted of driftscans covering an area of $0\farcm9 \times 3\farcm3$ ($0\farcm9 \times 7'$ for CTIO) oriented to coincide with the Spitzer IRS low-resolution maps, with multiple observations laid end to end to extend from the centers of the galaxies to $R \geq 0.5\,R_{25}$ (de Vaucouleurs et al. 1991). A summed spectrum was then extracted by integrating over this $0\farcm9$-wide strip. The areal coverage of these driftscan apertures ranged from <10% of the total projected region within R_{25} for the largest galaxies in the sample (e.g., M81), to nearly 100% for the smallest galaxies in the sample. We also obtained a separate drift-scanned spectra for the optical centers of each galaxy, using $20'' \times 20''$ apertures, to approximately match the coverage of a set of high spectral resolution *Spitzer* IRS observations. Again the two-dimensional spectra were collapsed into a single integrated spectrum covering the central aperture. A third set of (pointed) spectra just covering the galactic nuclei were also obtained. Those data are not used in this paper, apart from helping to classify the nuclear emission types, and checking to ensure that AGN emission does not dominate the other, larger-aperture spectra. The processing and emission-line extractions for these data followed the procedures described in MK06 and Moustakas et al. (2009), and the data can be found in the latter paper.

For some of the SINGS galaxies the drift-scanned spectra could not be used to reliably estimate the disk-averaged Hα/Hβ ratio, either because the Hβ line was too weak or because the spatial coverage of the spectra was too limited. For 23 of these cases spectra for individual HII regions were available from the literature, and we used these to estimate the disk-averaged Hα/Hβ ratio and its uncertainty. We checked the validity of this procedure by comparing

the mean Balmer decrements with those derived from drift-scanned spectra when both types of data were available, and they yield consistent results with no systematic bias, though with less precision than from the integrated spectra.

Table 1 lists the adopted Hα/Hβ ratios (and data sources) for the SINGS galaxies, and Table 2 lists the adopted Hα and Hβ fluxes for the MK06 galaxies.[3]

2.3. Integrated Hα Fluxes

Integrated Hα fluxes for the MK06 sample were taken directly from the drift-scanned integrated spectra. The same applied to the observations of the central $20'' \times 20''$ regions in the SINGS galaxies. In many cases integrated Hα fluxes for the SINGS galaxies had to be obtained from other sources, because of the incomplete spatial coverage of the drift-scanned spectra. Fluxes were compiled from the literature or were measured from Hα narrow band images obtained as part of the SINGS project.[4] Most of these measurements include emission from the neighboring [NII]$\lambda\lambda$6548,6584 lines. We applied [NII] corrections on a galaxy by galaxy basis, using the [NII]/Hα ratio measured in our drift-scanned spectra (26 galaxies), or individual measurements of disk HII regions in the galaxies from the literature (19 galaxies). For an additional 13 galaxies we applied the mean relation between average [NII]/Hα and M_B in the MK06 sample, as published in Kennicutt et al. (2008).

The accuracy of the individual Hα fluxes varies considerably, depending on the absolute and relative strength of the line (relative to continuum) and the source of the fluxes. A comparison of MK06 Hα fluxes with high-quality narrow-band imaging measurements by Kennicutt et al. (2008) shows that the average uncertainty of the fluxes is approximately $\pm$10% – 15%. This uncertainty could increase to as much as $\pm$30% for galaxies with weak emission or with a strong underlying continuum. Table 1 lists the adopted Hα fluxes and [NII]/Hα ratios for the SINGS sample.

2.4. Infrared Fluxes

For the SINGS sample we have used the integrated *Spitzer* measurements from Dale et al. (2007) at wavelengths of 3.6, 8.0, 24, 70, and 160 μm. We also used the SINGS images

[3]Full machine-readable versions of these tables can be found in the electronic version of the ApJ.

[4]SINGS data products including Hα images can be found at http://irsa.ipac.caltech.edu/data/SPITZER/SINGS/.

(Version DR5) to measure 8 μm and 24 μm fluxes with the same 20″ × 20″ circumnuclear apertures that were measured spectroscopically (§2.2, 2.3). We did not measure 70 μm or 160 μm fluxes for the circumnuclear apertures, because the instrumental beam sizes at those wavelengths were comparable to or larger than the apertures. We refer the reader to Dale et al. (2007) for a detailed listing and discussion of the uncertainties in these fluxes. Aperture corrections (including extended source corrections for scattering of diffuse radiation across the IRAC focal plane) were applied to the circumnuclear measurements, and amount to approximately 10% at 8 μm and 25% at 24 μm.

Most of the galaxies in the MK06 sample have not been observed with *Spitzer*, so we compiled integrated fluxes at 25, 60, 100 μm from the *IRAS* survey. Whenever possible we adopted in order of priority the fluxes measured in the *IRAS* Revised Bright Galaxy Sample (Sanders et al. 2003), followed by *IRAS* Bright Galaxy Sample (Soifer et al. 1989), then the large optical galaxy catalog (Rice et al. 1988) and finally Version 2 of the *IRAS* Faint Source Catalog (Moshir et al. 1990). For this study we are mainly interested in the 25 μm–band fluxes and the TIR fluxes. Many galaxies in the sample are undetected or have only marginal detections at 25 μm, and we restricted our analysis to galaxies with >3-σ detections at that wavelength. As a supplement to the *Spitzer* measurements we also compiled the same *IRAS* data for the SINGS sample. Of the 58 galaxies in our main *Spitzer* sample, 46 were observed by *IRAS* and satisfy our 25 μm signal/noise criterion.

A key SFR index in our analysis is the wavelength-integrated total infrared (TIR) luminosity. The *IRAS* and *Spitzer* photometry do not cover enough wavelengths to uniquely define this flux integral, with the emission longward of 100 μm and 160 um, respectively, being especially poorly constrained. As a result there are numerous prescriptions in the literature for computing a TIR flux from the *IRAS* and *Spitzer* band fluxes. For the sake of consistency we have adopted the definition of TIR flux from Dale & Helou (2002), which is the bolometric infrared flux over the wavelength range 3—1100 μm. We also adopt the semi-empirical prescriptions from that paper for estimating $f(TIR)$ from weighted sums of MIPS 24, 70, and 160 μm fluxes (equation [4] of their paper), and from IRAS 25, 60, and 100 μm fluxes (equation [5] of their paper).

It is important to test the consistency of the *IRAS* and *Spitzer* flux scales, and since the SINGS sample was measured with both sets of instruments they provide a direct standard for this comparison. We first compared the consistency of the *Spitzer* MIPS photometry at 24 μm with the *IRAS* 25 μm fluxes, using the common definition of monochromatic flux $f(\lambda) = \nu f_\nu$. The left panel of Figure 1 shows the ratio of MIPS/*IRAS* fluxes as a function of 24 μm flux. Overall the flux scales are in excellent agreement, with an average ratio $f(MIPS)/f(IRAS)$ = 0.98 ± 0.06 after the 3-σ outliers were excluded. The three outliers are faint and/or low

surface brightness IR emitters with single published *IRAS* flux measurements. Apart from these isolated examples we find that the MIPS 24 μm and *IRAS* 25 μm fluxes can be used interchangeably. For the sake of simplicity we shall use the terms "24 μm fluxes" and "24 μm luminosities" to refer to measurements made either at 24 μm or 25 μm.

The right-hand panel of Figure 1 shows the ratio of MIPS and *IRAS* TIR fluxes. Both sets of fluxes were computed using the prescriptions of Dale & Helou (2002). Here the deviations are larger, with a scatter of $\pm 23\%$ and a systematic offset of 24% in flux scales (MIPS larger). This offset is considerably larger than the uncertainty given by Dale & Helou (2002). To better understand this discrepancy we compared our flux ratios $\mathrm{f(TIR)}_{MIPS}/\mathrm{f(TIR)}_{IRAS}$ as a function of FIR color $\mathrm{f}_\nu(60\,\mu\mathrm{m})/\mathrm{f}_\nu(100\,\mu\mathrm{m})$, as shown in Figure 2. For galaxies with warm IR colors (high $\mathrm{f}_\nu(60\,\mu\mathrm{m})/\mathrm{f}_\nu(100\,\mu\mathrm{m})$ ratios), the SED peaks near or shortward of 100 μm, so the 25, 60, and 100 μm IRAS fluxes provide a relatively reliable estimate of the integrated TIR flux. However for galaxies with colder colors $[f_\nu(60\,\mu\mathrm{m})/f_\nu(100\,\mu\mathrm{m}) < 0.4]$, the peak of the SED is longward of 70 μm, so there is more of a danger of systematic uncertainties affecting the TIR flux estimates. The solid line in Figure 2 shows the approximate magnitude of this error predicted by the Dale & Helou (2002) SED models. The actual comparison for the SINGS galaxies displays the sense of this predicted trend, but the systematic differences between MIPS and *IRAS* measurements is more severe. This comes about because the SINGS sample included a number of galaxies with colder dust than any of the galaxies in the template reference sample explored by Dale & Helou (2002). For that reason we analyze the *Spitzer* and *IRAS* TIR data separately in the analyses that follow.

2.5. Radio Continuum Fluxes

In §5.3 of this paper we explore whether the integrated (mainly non-thermal) radio continuum fluxes of galaxies can be combined in the same way with optical emission-line fluxes to provide attenuation-corrected SFRs. Radio continuum fluxes at 1.4 GHz for the SINGS sample were taken from the compilation of Dale et al. (2007). To obtain a matching set of radio data for the MK06 sample we cross-correlated the galaxies with the NRAO VLA Sky Survey (NVSS; Condon et al. 1998). After experimenting with several choices of matching radii we used a radius of 20″, which provided the optimal yield of matched sources without introducing significant numbers of spurious matches with background sources. This produced radio fluxes for 100 of the 113 star-forming galaxies in the MK06 sample. We also used pointed observations of 32 galaxies from Condon (1987), and adopted them in preference to the NVSS when both sets of measurements were available, to minimize problems with missing extended flux in the NVSS data (Yun et al. 2001).

3. INTEGRATED Hα + IR INDICES

Our method for using linear combinations of Hα and IR (specifically, 24 μm) fluxes to derive attenuation-corrected Hα luminosities was introduced in previous SINGS papers by Calzetti et al. (2007), Prescott et al. (2007), and Kennicutt et al. (2007), and applied to measurements of HII regions and HII region complexes. Here we describe the physical basis for the method in more depth, and adapt it for measurements of galaxies, where there are contributions to dust heating from a much wider range of stellar ages than in HII regions.

3.1. Methodology

Our method uses the IR luminosities of galaxies to estimate attenuation corrections for their optical emission-line (or ultraviolet continuum) luminosities. Its physical basis is a simple energy balance argument (see Inoue et al. 2001 and Hirashita et al. 2003 for similar approaches to this problem). We assume that on average the attenuated luminosity in Hα is re-radiated in the infrared, with a scaling factor that is calibrated empirically, and will differ depending on the IR emission component used and secondarily on the nature of the dust-heating stellar population. Following Kennicutt et al. (2007), we can construct a linear combination of the observed Hα and IR luminosities that reproduces the true unattenuated Hα luminosity:

$$L(H\alpha)_{corr} = L(H\alpha)_{obs} + a_\lambda L(IR) \tag{1}$$

where $L(H\alpha)_{corr}$ and $L(H\alpha)_{obs}$ denote the attenuation-corrected and observed Hα luminosities, respectively, $L(IR)$ represents the IR luminosity over a given wavelength bandpass, and a_λ is the appropriate scaling coefficient for that wavelength band and dust heating population. The equivalent attenuation correction for Hα is simply:

$$A(H\alpha) = 2.5 \log[1 + \frac{a_\lambda L(IR)}{L(H\alpha)_{obs}}]. \tag{2}$$

Equations (1) and (2) represent simple approximations to a much more complicated dust radiative transfer process in galaxies (e.g., Witt & Gordon 2000, Charlot & Fall 2000), but their physical motivation can be readily understood as follows. We first define a scaling factor η that represents the fraction of the bolometric luminosity of a stellar population that is reprocessed as Hα emission in a surrounding ionization-bounded HII region:

$$L(H\alpha)_{corr} = \eta L_{bol} \tag{3}$$

where as before $L(H\alpha)_{corr}$ represents the intrinsic (extinction-free) Hα luminosity and L_{bol} represents the bolometric stellar luminosity of the same region. Considering now explicitly the attenuation of the emission line, its attenuated luminosity can be expressed as:

$$L(H\alpha)_{obs} = L(H\alpha)_{corr}\, \mathrm{e}^{-\tau_\lambda} \tag{4}$$

The attenuation in magnitudes $A(\lambda) = 1.086\,\tau_\lambda$. The IR luminosity for the region (consider for example the total wavelength-integrated IR luminosity) likewise can be expressed as:

$$L(TIR) = L_{bol}\,(1 - \mathrm{e}^{-\overline{\tau}}) \tag{5}$$

where the relevant opacity in this case is the effective (absorption and luminosity-weighted) opacity of the starlight heating the dust.

$$\bar{\tau} = -\ln \frac{\int L_\lambda e^{-\tau_\lambda} d\lambda}{\int L_\lambda d\lambda} \tag{6}$$

This mean opacity depends on the wavelength dependence of the attenuation, the spectral energy distributions of the stars that heat the dust, and the dust covering factors for these stellar populations. In general it will *not* necessarily be the same as the dust opacity τ_λ for the emission line of interest. We can substitute eqs. (4) and (5) into eq. (3) to eliminate L_{bol} and express $L(H\alpha)_{corr}$ in terms of the observable luminosities $L(H\alpha)_{obs}$ and $L(TIR)$ and the opacities. It is convenient to introduce a scaling parameter β, the ratio of the emission-line opacity to effective mean stellar opacity for the stars heating the dust:

$$\beta \equiv \frac{\tau_\lambda}{\overline{\tau}} \tag{7}$$

then eq. (1) takes the modified form:

$$L(H\alpha)_{corr} = L(H\alpha)_{obs} + \eta L(TIR)\,\frac{(1 - \mathrm{e}^{-\beta\overline{\tau}})}{(1 - \mathrm{e}^{-\overline{\tau}})} \tag{8}$$

In detail the opacity index β depends on several parameters, most importantly the wavelength of the optical (or UV) SFR tracer, but also on the overall stellar population mix and the distribution of dust opacities for different age populations, all which will influence $\overline{\tau}$.

These relations take a much simpler form in the special situation where $\tau_{H\alpha} \simeq \overline{\tau}$ (i.e., $\beta \simeq 1$). In that case the opacity term in eq. [8] drops out, and we are left with the simple result:

$$L(H\alpha)_{corr} = L(H\alpha)_{obs} + \eta L(TIR) \tag{9}$$

the same as eq. (1) with coefficient $a_\lambda = \eta$, the bolometric correction term for $L(H\alpha)$. If this approximation holds then the attenuated-corrected emission-line luminosity can be derived from a linear combination of the observed Hα luminosities and the TIR (or other IR) luminosity.

Thanks to fortuitous physical circumstances this approximation is valid for the Hα emission line. Although the line is emitted in the red (0.6563 μm), observations show that the dust attenuation of galaxies in the Balmer lines is approximately 2.3 times higher than the corresponding attenuation in the stellar continuum (see Calzetti 2001 and references therein). As a result the attenuation of the Hα line is comparable to that of the stellar continuum in the 0.3–0.4 μm range, close to where the peak contribution to dust heating occurs in most galaxies (Calzetti 2001). Below in §3.3 we use the spectral energy distributions of the galaxies in our sample to confirm this quantitatively.

We can also use the results presented above to explore the validity of applying a linear combination of emission-line and IR fluxes (eq. [1]) in the more general case when the line attenuation is systematically larger or smaller than the mean opacity to the dust-heating starlight. This would be the case for emission lines at much shorter or longer wavelengths than Hα, or even for Hα itself, if the dust-heating starlight was dominated by extremely young (i.e., blue) or old (i.e. red) stellar populations. In such cases the re-emitted starlight in the dust continuum will tend to under-compensate or over-compensate for the flux attenuated in the emission line. The magnitude of this effect can be calculated using eq. (8). Figure 3 plots the ratio of the attenuation-corrected luminosity estimated from naive application of eq. (1) to the actual intrinsic luminosity, for six values of β in the range 0.25 – 2 (the solid line at unity is the case for $\beta = 1$). The systematic error reaches its maximum value for optical depths of 0.7 – 2 (approximately the same range in magnitudes). For most combinations of β and opacity the systematic errors are small, of order 10–20%, when compared to other systematic uncertainties in the determination of the SFRs. The mismatch in opacities is also unimportant for low optical depths, because in those situations the emission contribution from the IR is negligible. The values of β shown in Figure 3 covers a wide range of potential emission lines from Pa α at 1.89 μm ($\beta \sim 0.25$) to [O II]λ3727 ($\beta \sim 2$). In this paper we shall apply the linear relations in eqs. (1) and (2), and use comparisons to independent measurements of attenuation-corrected SFRs and attenuations to evaluate the efficacy of

the method.

3.2. Reference SFRs

Our method in effect uses the ratio of infrared to Hα fluxes of galaxies to derive attenuated-corrected Hα luminosities and SFRs. These need to be calibrated using independent measurements of the Hα attenuation corrections. For the latter we have chosen to use the stellar-absorption corrected Hα/Hβ ratios from our integrated spectra, converted to Hα attenuations using a Galactic extinction curve. Specifically, we assume an intrinsic Hα/Hβ ratios for Case B recombination ($I(H\alpha)/I(H\beta) = 2.86$) at electron temperature T_e = 10,000 K and density N_e = 100 cm^{-3} (Hummer & Storey 1987). The dust attenuation curve of O'Donnell (1994) was used to convert the observed reddenings to attenuation values at Hα ($R_V = 3.1$). The latter is equivalent to adopting a Galactic dust extinction curve, and assuming a foreground dust screen approximation for the attenuation correction in the Balmer lines. We discuss the possible limitations of these assumptions below in §3.3 and in §6.3.

3.3. Physical Assumptions and Limitations

As emphasized earlier our simple energy balance method is an idealized prescription that approximates a much more complicated radiative transfer problem in galaxies, and it is important to bear in mind and quantify any systematic errors and limitations that may be introduced by these approximations. The most important of these approximations are: 1) assumption of comparable extinction in the optical emission-line tracer and in the dust-heating continuum; 2) assumption of isotropic dust geometry; 3) adoption of an average dust-heating stellar population mix across the sample; 4) assumption of a reliable set of reference SFRs and attenuation measurements, which are free of dust-dependent systematic errors. We defer a full discussion of these assumptions and any associated uncertainties to §6, after the main results have been presented. However we briefly address the points here, to offer reassurance that the assumptions are reasonable for the current application.

As shown earlier the use of linear combination of Hα and IR SFR tracers to derive attenuation-corrected SFRs is strictly valid in the case where the averaged dust attenuations in Hα and the dust-heating stellar continuum are comparable. The attenuation laws of Calzetti (2001, and references therein) show that this is a plausible assumption, but we can test it directly. We combined measurements of the galaxies in MK06 sample from the Galaxy

Evolution Explorer (GALEX; Martin et al. 2005), the Two Micron All Sky Survey, and the Sloan Digital Sky Survey (SDSS; Adelman-McCarthy et al. 2006) to derive the bolometric luminosities of the galaxies, exclusive of the re-emitted dust luminosities. The ratio of these luminosities to the total-infrared luminosities were then used to derive an estimate of $\overline{\tau}$ for each galaxy, using eq. (5). These values were then compared in turn to measurements of $\tau_{H\alpha}$ from the Balmer decrements. Figure 4 shows a histogram of the resulting values of $\beta = \tau_{H\alpha}/\overline{\tau}$. The median value of $\beta = 1.08$, which is consistent with unity within the uncertainties in the optical depths. Much of the dispersion in values is physical, and reflects differences in SED shape within the sample (B. Johnson et al. 2009, in preparation). The result justifies the use of the linear approximation, at least for combinations of Hα and IR fluxes, and of course for combinations of UV continuum and IR fluxes (Paper II).

Variations in dust geometry will be another source of uncertainty in the IR-based attenuation corrections. Our model assumes an isotropic distribution of dust around the stars, but we expect few regions to adhere to this idealized geometry. So long as there is no systematic bias toward foreground or background dust in galaxies we do not expect this to introduce significant systematic errors, but geometry variations may introduce a significant random error into individual determinations of attenuation. When C07 applied our method to 220 bright HII regions in 33 SINGS galaxies, they found excellent consistency between the derived Hα attenuations and those derived from Pa$\,\alpha$/Hα ratios, but with a dispersion of $\pm$0.3 dex for individual objects. This factor-of-two dispersion is consistent with the combined effects of varying dust geometry and stellar population in the HII regions. We might well expect the dispersions to be lower for galaxies, where we are integrating over hundreds to thousands of individual star-forming regions.

As will be discussed further in §6 variations in dust-heating stellar populations– the longstanding "infrared cirrus" problem, is probably the largest source of systematic uncertainty in this approach. The dust heating in galaxies arises from a much larger range of stellar ages (and dust heating geometries) than in the HII regions and starbursts studied by C07, so the calibration coefficients in eq. (1) derived by C07 are not expected to apply to the measurements of galaxies as a whole. Comparing the results for galaxies and HII regions will provide an indirect measure of the relative contributions of heating from very young (<10 Myr old) and older stars, and some indication of the uncertainties in SFRs when different types of galaxies are compared.

Finally, any systematic error in the reference attenuations derived from Balmer decrements will propagate with full weight into our calibrations. Our approximation to dust with a Galactic extinction curve in the foreground screen limit is the most common convention for analyses of both HII region spectra and integrated spectra of galaxies (see Calzetti 2001 and

references therein), but its use raises some legitimate questions. A large body of theoretical studies of dust radiative transfer in galaxies (e.g., Witt & Gordon 2000, Charlot & Fall 2000, Charlot & Longhetti 2001, Tuffs et al. 2004, Jonsson et al. 2009) show that the actual relation between the reddening of an integrated spectrum and its dust attenuation can vary considerably, depending on the dust geometry and the relation between extinction and stellar age. In galaxies with severe dust extinction, such as in many ULIRGs, these geometric effects will cause the Balmer decrement to be biased to the least obscured regions, leading to a systematic underestimate of the actual attenuation. The predictions for more typical disk galaxies are inconclusive, with some studies suggesting a mild bias in attenuations estimated from the foreground dust screen approximation (e.g., Charlot & Fall 2000), but with other studies showing little or no bias (e.g., Jonsson et al. 2009). However observations at other wavelengths (Pa α, thermal radio continuum, and UV+IR) allow us to independently derive Hα attenuation estimates for subsets of our sample, and test for systematic errors in the zero-point of our Balmer decrement based attenuation scale. As shown in §6.3 these tests confirm the reliability of the Balmer attenuation scale at the $\pm$10–20% level, which is comparable to other systematic errors in our SFR scales. On that basis we have chosen to use the Balmer decrements with the most commonly applied attenuation correction procedures. We also publish the observed Balmer line ratios so other workers may apply alternative attenuation corrections in the future.

4. APPLICATION TO INTEGRATED MEASUREMENTS OF GALAXIES

In this section we use the combination of Hα fluxes, IR fluxes, and optical spectra for our galaxies to examine the consistency of SFRs measured from Hα and IR tracers, and to calibrate composite SFR indices. Since this work originally grew out of the discovery of a strong correlation between Hα and 24 μm emission in HII regions, we first extend this calibration to galaxies. We then calibrate a similar combination of Hα and TIR luminosities (not possible for the SINGS HII regions due to the limited spatial resolution of the far-IR data). The section concludes with an analysis of systematic residuals in the SFR calibrations as functions of various properties of the galaxies and their SEDs.

4.1. Combinations of Hα and 24 μm Measurements

As an introduction it is instructive to compare the consistency of Hα and IR SFR measures before any corrections for attenuation are applied. Figure 5 compares the observed Hα luminosities of the SINGS and MK06 galaxies with their corresponding 24 μm

($\nu\, f_\nu$) luminosities. When converting fluxes to luminosities we have used distances listed for SINGS galaxies in Table 1, and from MK06 in Table 2. Both sets of distances assume $H_0 = 70\,\mathrm{km\,s^{-1}\,Mpc^{-1}}$ with local flow corrections. In Figure 5 (only) we do not distinguish SINGS galaxies from MK06 galaxies and we code the points by spectral type, with open round points representing galaxies dominated by star formation, crosses representing galaxies with strong AGN signatures in their spectra, and circles with embedded crosses denoting composite AGN and star formation dominated spectra. The axis label along the top of the plot shows the corresponding SFR (uncorrected for attenuation), using the calibration of K98. Finally, the solid line shows a linear (unity slope) relation for reference, with the zero-point set to match the mean relation between L(24 μm) and $\mathrm{L(H}\alpha)_{\mathrm{corr}}$ found by Zhu et al. (2008) for nearby galaxies in the *Spitzer* Wide-Area Infrared Extragalactic (SWIRE) survey (Lonsdale et al. 2003).

The Hα and 24 μm luminosities show a broad correlation, as is often the case when absolute luminosities are compared. Upon closer examination, however, important departures are apparent. The rms dispersion around the linear relation is $\pm$0.5 dex, more than a factor of three. Part of this dispersion is caused by AGN contributions to the dust emission. The galaxies with significant AGN contributions clearly are displaced in the diagram, reflecting in part the additional dust heating by the active nuclei (e.g., Soifer et al. 1987). Since we are solely interested in calibrating SFR tracers we shall exclude galaxies with strong AGN signatures from most of the subsequent analysis in this paper, but clearly the issue of AGN contamination is always an important one when applying any SFR tracer. Even among the star-forming galaxies, however, the dispersion about the linear relation is large, approximately $\pm$0.4 dex. The dispersion among these galaxies is caused almost entirely by variations in dust attenuation; the observed Hα flux underestimates the SFR in dusty galaxies, while the IR emission underestimates the SFR in less dusty galaxies. Moreover, the relation between Hα and IR emission clearly is nonlinear, with the mean ratio of IR to Hα luminosities increasing by a factor of 30 from the faintest to the most luminous galaxies in the sample. This nonlinearity is a manifestation of the well established relation between attenuation and SFR (e.g., Wang & Heckman 1996). Higher SFRs are associated with regions of higher gas surface density (Kennicutt 1998b, C07) and hence higher dust column densities. As a result galaxies with the highest SFRs tend to suffer heavy attenuation, and the observed Hα flux severely under-represents the actual SFR, moving points in Figure 5 to the left. Likewise many (but not all) of the galaxies with low SFRs tend to be low-mass galaxies with lower dust contents and column densities. For those objects the attenuation at Hα is low and the emission line provides an accurate measure of the SFR, but then the dust emission severely under-represents the SFR, shifting points down in Figure 5.

We can remove the part of the nonlinearity in Figure 5 that is produced by attenua-

tion of Hα by comparing instead the 24 μm luminosities with the attenuation-corrected Hα luminosities, as derived from the Balmer decrements in the integrated spectra (§3.2). This comparison is shown in the top panel of Figure 6 (now with the AGN-dominated and composite spectrum galaxies removed). Here and throughout the paper integrated measurements of SINGS galaxies are shown as open circles, and those for the MK06 sample are shown as solid circles. Applying the reddening corrections tightens the correlation with 24 μm emission considerably, but the dispersion about the mean relation remains substantial at $\pm$0.3 dex, and the nonlinearity remains. Nearly all of the scatter and nonlinearity in this relation are caused by variations in the fraction of young starlight that is reprocessed by dust.

Previously several groups have investigated the correlation between 24 μm IR emission and attenuation-corrected Hα and Pa α emission, and used them to calibrate the 24 μm emission as a SFR measure (Wu et al. 2005, Alonso-Herrero et al. 2006, Relaño et al. 2007, C07). The relations from Wu et al. (2005), Relaño et al. (2007), and C07 can be directly compared to our data, as shown in the top panel of Figure 6. Apart from slight deviations at the extremes in luminosity our data generally follow these relations as well. Nevertheless it is dangerous to use the IR luminosity by itself as a quantitative SFR tracer, because in any galaxy other than an extremely dusty starburst the dust reprocesses only a fraction of the young starlight, and any linear scaling of a SFR calibration based on dusty starburst galaxies will tend to systematically under-estimate the SFR in lower-luminosity normal galaxies. This is shown by the dotted line in the top panel of Figure 6, which shows a linear (slope unity) relation fitted to the data. The calibrations of Wu et al. (2005) and Relaño et al. (2007) mitigate this effect by fitting a nonlinear relation between $L(24)$ and $L(H\alpha)$, which effectively builds in a decrease in mean attenuation with decreasing SFR. However it represents a crude, unphysical correction at best. While most present-day galaxies with low Hα luminosities tend to be dwarf galaxies with low dust contents and optical depths, this same range of fluxes is occupied by dusty galaxies with low SFRs (mostly early-type spirals); attenuation does not correlate monotonically with the SFR itself. Thus while nonlinear calibrations of the 24 μm luminosity may provide crude statistical measures of the SFR, the uncertainties associated with measurements of individual galaxies remain very high. One risks even larger, systematic errors if one were to apply such relations at high redshift, because there is no reason to expect that the relations between mean attenuation and SFR observed at $z = 0$ necessarily apply in the early universe.

However we can mitigate the effects of variable attenuation between the galaxies by applying eq. (1), using a linear combination of the observed (uncorrected) Hα and mid-IR luminosities to estimate the attenuation-corrected Hα luminosity. The result is shown in the bottom panel of Figure 6, which compares the corrected Hα luminosities derived from the ratio $L(24)/L(H\alpha)_{obs}$ with those derived from the Balmer decrements. We fitted

for the value of the scaling factor a in eq. (1) that provides the best overall agreement with the luminosities corrected from the Balmer decrements ($a = 0.020 \pm 0.001_{\rm r} \pm 0.005_{\rm s}$), where the first error term lists the formal (random) fitting uncertainty, and the second term includes possible systematic errors in the calibration zeropoint including any uncertainty in the reference attenuation scale based on Balmer decrement measurements (see §6.3). We shall adopt this convention of citing both random and systematic errors throughout the remainder of this paper.

The consistency between the two independent sets of attenuation-corrected Hα luminosities is striking, as is the decrease in the dispersion between the two SFR estimates, relative to the comparisons of 24 μm vs Hα luminosities alone in the top panel of Figure 6. This is especially apparent for the galaxies with $L(H\alpha) < 10^{42}$ ergs s^{-1}. The galaxies with the lowest luminosities tend to have very little dust, and hence nearly no reddening and only weak IR emission. In such galaxies the Hα luminosity dominates the sum in eq. (1). On the other hand most of the galaxies with $L(H\alpha) > 10^{42}$ ergs s^{-1} in Figure 6 are LIRGs, with very high attenuations. In such cases it is the IR term in eq. (1) that dominates the sum.

Our fitted value of the coefficient a in eq. (1) is 35% lower than the value $a = 0.031 \pm 0.006$ derived by C07 based on measurements of HII regions in SINGS galaxies. However our value is in excellent agreement with $a = 0.022$ derived by Zhu et al. (2008) for a sample of luminous star-forming galaxies observed in common between the SWIRE survey and the SDSS. We believe that the difference in scaling coefficients is consistent with expectation given the different stellar age distributions in HII regions and galaxies, as discussed in §6.

4.2. Combinations of Hα and Total Infrared Measurements

Before examining the implications of Figure 6 in more depth we can make the same comparison, but combining instead the Hα and TIR luminosities of the galaxies. The results are shown in Figure 7. As before the top panels show the TIR luminosity as a function of $L(H\alpha)_{\rm corr}$, while the bottom plots show the linear combination of TIR and Hα luminosities (in this case with the fitted $a = 0.0024 \pm 0.0001_{\rm r} \pm 0.0006_{\rm s}$). Because of the systematic differences between MIPS and *IRAS* TIR scales we separate these data in Figure 7, with the left panels showing *Spitzer* MIPS-based TIR luminosities (SINGS sample) and the right panels showing *IRAS*-based luminosities (SINGS and MK06 samples). Since MIPS observations are not available for most of the MK06 sample most of the TIR data used in the remainder of this paper will be based on *IRAS* luminosities, to maximize the uniformity of the data. However the more sensitive MIPS data allow us to extend the range of luminosities covered by nearly an order of magnitude.

The most gratifying result shown in the bottom panel of Figure 7 is not the linearity of the relation (which is dictated by the fitting of a) but rather the tightness of the relation. To illustrate this better Figure 8 shows the residuals from the fits in Figure 6 (left panels, $24\,\mu$m and Hα) and Figure 7 (right panels, *IRAS* TIR and Hα). The combination of Hα and IR flux dramatically improves the consistency and tightness of both relations. In both cases these dispersions are less than half of the rms (logarithmic) deviations when the IR luminosities by themselves are compared to the Balmer-corrected luminosities. We suspect that the tighter residuals in the Hα + TIR index ($\pm$0.09 dex rms vs $\pm$0.12 dex for H$\alpha + 24\,\mu$m) reflect the higher quality of the longer wavelength IRAS measurements as well as lower sensitivity to local variations in dust heating (see §6 for further discussion). The lack of any systematic residual with total luminosity (and thus SFR) is also significant, and argues against any large systematic error in the derived values of the fitting coefficients a.

Figures 5–7 compare absolute luminosities in various wavelengths, and it is well known that such plots can sometimes mask underlying physical trends, because of the large range in galaxy masses that underlies any comparison of absolute quantities. These effects can be removed by analyzing mean surface brightnesses (which scale with the SFR per unit disk area) instead of luminosities. For this comparison we defined the disk area as the deprojected area of the spectroscopic aperture for the MK06 galaxies, and area within the R_{25} radius (de Vaucouleurs et al. 1991) for the SINGS galaxies. These provide only approximate measures of the radii of the star-forming disks (e.g., Kennicutt 1989, 1998b), but they suffice for this statistical comparison. The top panels of Figure 9 show that the same trend we observed in disk opacity functions of luminosity are also seen in SFR per unit area. This is not surprising, because it is well known that the SFR per unit area correlates strongly with the average surface density of gas (e.g., Kennicutt 1998b), and it stands to reason that it would correlate with the mean column density of dust as well. The bottom two panels show that our prescriptions for correcting the Hα emission for attenuation using IR observations are in excellent agreement with the Balmer-derived attenuations over the full range (more than a factor of 1000) in Hα surface brightness.

Finally, Figure 10 compares the Hα attenuation estimates themselves. The left and right panels compare the Hα attenuations derived using Hα + $24\,\mu$m and Hα + TIR luminosities, respectively, with those derived from the spectroscopic Hα/Hβ attenuation values. The solid line in each panel shows the line of equality, while the dotted lines on either side contain 68% of the points ($\sim$1-σ; the overall dispersions are identical to those in the previous figure). Overall there is excellent consistency between the attenuation estimates. The outliers tend to be SINGS galaxies where spatially undersampled spectroscopic strips do not provide a representative measure of the global reddening, along with a few galaxies with deeply embedded central star-forming regions. Overall, however, the attenuation estimates,

especially those derived from the combination of Hα and TIR luminosities, show impressive consistency with the spectroscopic reddening-derived attenuations, given that the methods are entirely different.

The consistency between the IR-derived and Balmer-derived attenuations for the integrated measurements of the SINGS and MK06 galaxies is also much tighter than for comparable measurements of individual giant HII regions. C07 applied the same methodology to Spitzer 24 μm and Hα measurements of 220 HII regions and star-forming complexes in 33 SINGS galaxies, compared these to attenuations derived from Paα/Hα ratios, and derived a mean dispersion of $\pm$0.3 dex (a factor of two) about the mean relation. A similar comparison of a homogeneous set of data for 42 HII regions in M51 by Kennicutt et al. (2007) yielded a dispersion of $\pm$0.25 dex. For the integrated measurements in this paper we find a corresponding dispersion of $\pm$0.12 dex between 24 μm + Hα and Hα/Hβ measurements, and even less for the TIR + Hα and Balmer-derived attenuations. Zhu et al. (2008) made a similar comparison of attenuated-corrected luminosities based on 24 μm + Hα and Hα/Hβ measurements for their SWIRE+SDSS sample. They do not quote a dispersion, but based on their Figure 5 we estimate that it is approximately $\pm$0.14 dex, somewhat larger than our result, but understandable in view of the uncertainties in the large aperture corrections that were required to match the SDSS fiber fluxes to the Spitzer 24 μm observations. The larger residuals in the HII region results may be caused in part by larger measuring uncertainties in the Paα and Hα photometry of the HII regions; however we would also expect physical effects such as variations in attenuation geometry and age variations in the HII regions to produce larger residuals. These latter effects tend to average out when integrated over an entire galaxy's population of star-forming regions.

4.3. Systematic Effects and Second-Order Correlations

The correlations between the IR-based and optically-based attenuation measurements are so tight that it is worthwhile investigating whether the residuals from these relations vary systematically with the SEDs or physical properties of the galaxies. As with any quantitative star formation tracer it is important to establish the limiting range of SFRs and galaxy types over which these methods can be applied reliably, and assess whether they can be extrapolated to galaxy types outside of our sample, for example the extremely luminous star-forming galaxies observed at high redshift.

We tested for systematic residuals against eight parameters, including SFR (Figure 8), SFR per unit area (cf. Figure 9), and six other parameters shown in Figures 11 and 13. Figure 11 shows the logarithmic residuals of attenuation-corrected Hα luminosities derived from

H$\alpha + 24\,\mu$m (left) and H$\alpha +$ TIR (right), relative to those derived using the Balmer decrement, plotted as functions of FIR 60 μm to 100 μm flux ratio (top panel), Balmer-derived attenuation (middle panel), and axial ratio or inclination (bottom panel). The only significant trends seen are a systematic residual in Hα + 24 μm-based SFRs with $f_\nu(60\,\mu\mathrm{m})/f_\nu(100\,\mu\mathrm{m})$ ratio and Balmer attenuation. This trend with IR color is a byproduct of the systematic variation in infrared SED shapes of galaxies; galaxies with higher 60 μm to 100 μm flux ratios also show higher L(24 μm)/L(TIR) (or L(25 μm)/L(TIR)) ratios. This well-known trend is illustrated for our sample in Figure 12, with the sequence of SED models by Dale & Helou (2002) superimposed. As a result we believe that the trend in residuals in the upper left-hand panel of Figure 11 is an artifact of the variation in SED shapes of galaxies, and this contributes considerably to the larger scatter in this index relative to a linear combination of Hα and TIR luminosities. Interestingly the latter residuals show no systematic trend with galaxy IR SED shape.

The trend in residuals with Balmer attenuation (middle left panel of Figure 11) is less straightforward to interpret. Interestingly the sense of the trend is that galaxies with the highest Balmer attenuations have *weaker* 24 μm emission than expected, which is in the opposite sense of what one might expect if the Balmer decrements systematically underestimated the true attenuation in more dusty environments. The same trend is present in the Hα + TIR residuals (middle right panel), but is considerably weaker. This suggests that much of the trend in the middle left panel may be the byproduct of a second-order correlation between average dust temperature (i.e., mix of warm star-forming regions and background cirrus emission) and characteristic opacity of those regions (Dale et al. 2007), but this should be regarded as speculation rather than an explanation.

Interestingly neither set of IR-based attenuation and SFR estimates shows any systematic residual with Balmer attenuation/SFR as a function of axial ratio. One would not expect the Hα + IR (24 μm or TIR) indices to show any systematic effects with disk inclination, but one might imagine that the Balmer-based measurements would suffer from such a systematic effect. We do know that the Hα surface brightnesses of disks do decrease systematically with increasing inclination (Young et al. 1996), and our results suggest that this increase in attenuation is largely accounted for in both the IR-based and spectroscopic attenuation corrections. This offers some support for the robustness of the Balmer-based attenuation measurements.

Figure 13 shows the same residuals as Figure 11, but plotted this time as functions of three measures of the stellar populations in the galaxies, the integrated Hα equivalent width (EW) of the galaxies, the 4000 Å spectral break strength (Bruzual 1983, as applied by Balogh et al. 1999), and the gas-phase oxygen abundance ($12 + \log(O/H)$) estimated

from the nebular lines (Moustakas et al. 2006, 2009). The Hα EWs (top panels) roughly scale with the SFR per unit stellar mass (specific SFR). The residuals show no systematic change with EW over a very large range (5 Å − 230 Å), which includes galaxies with Hubble types Sb–Irr (K98). The bottom panels of Figure 13 show that there is no significant trend in attenuation residuals with metallicity.

The $D_n(4000)$ break provides a reddening-insensitive measure of the relative age of the stellar population in the galaxies (e.g., MacArthur 2005; Johnson et al. 2007b), and we might expect it to correlate with the attenuation residuals, if variations in heating of dust from evolved stars is important. A trend is seen in the Hα + 24 μm residuals (left middle panel of Figure 13), but we believe that this is mainly a second-order consequence of the IR SED dependence discussed earlier. There is no discernible trend in Hα + TIR attenuation residuals with $D_n(4000)$. One might have expected some deviation for the reddest galaxies with larger values of $D_n(4000)$, as the result of dust being heated primarily by evolved stars. Evidence for such deviations has been seen in comparisons analyses of UV and IR-based SFR tracers (e.g., Johnson et al. 2009; Cortese et al. 2008). We believe that two effects contribute to this negative result. One is the limited range in stellar population probed by this sample ($D_n(4000) \leq 1.4$). The other reason is a compensation between two physical effects; in galaxies with redder stellar populations there will be a stronger radiation component from evolved stars, but the radiation will also be shifted to longer wavelengths where the dust opacity is lower. In terms of eq. (8) in §3.1, there are changes in the coefficients η and β which tend to compensate for each other.

An alternate way to examine the residuals is to calculate for each individual galaxy a value of the IR/Hα scaling factor in eq. (1) that forces the derived reddening to match that derived from the Balmer decrement:

$$a_\lambda = \frac{L(H\alpha)}{L_\lambda(IR)} \, [10^{0.4 A_{Balmer}(H\alpha)} - 1] \tag{10}$$

We expect these individual values of a to show a considerable dispersion, especially in galaxies with relatively low attenuation, where the uncertainties in single attenuation estimates may be comparable to the estimates themselves. Figure 14 shows histograms of a_{24} and a_{TIR} for the integrated measurements of SINGS and MK06 samples, with the adopted average fits for the combined sample shown by vertical lines. There are a few prominent outliers in both cases, and these provide valuable examples of when our attenuation measures break down. For the outliers with anomalously high values ($a_{24} > 0.05$ and $a_{TIR} > 0.004$) the IR emission is considerably weaker than expected from the Balmer decrement. These tend to be either galaxies with low attenuation and IR emission, where the predicted IR emission is

sensitive to small uncertainties in the Balmer decrement, or cases where the limited spatial sampling of the SINGS spectroscopy does not provide an accurate measure of the global reddening. The points with anomalously low values of a include metal-poor galaxies with low attenuations, objects with deeply embedded star-forming regions, or other cases where the SINGS spectra probably under-estimate the global reddening of the galaxy, because the optical emission does not penetrate into the main IR-emitting region.

5. Composite SFRs with Other Emission Lines and IR Bands

We have shown that Hα fluxes of galaxies can be combined with either 24 μm or TIR fluxes to provide robust attenuation-corrected Hα luminosities and SFRs. Can other combinations of optical emission lines and infrared or radio continuum bands be used in the same way? In this section we extend our approach to the use of the 8 μm (PAH-dominated) band to derive attenuation-corrected Hα luminosities, the use of [O II]λ3727 + IR indices in place of Hα composite measures, and the combination of optical emission-line and radio continuum measurements. The combination of ultraviolet and IR luminosities is a mature subject in its own right and is analyzed separately in Paper II.

5.1. Hα and 8 μm Indices

With the advent of large-scale galaxy surveys with *Spitzer* there is growing interest in calibrating the rest 8 μm mid-IR luminosities of galaxies as quantitative SFR tracers. Most galaxies exhibit strong emission in the rest 8 μm band, and this wavelength region redshifts into the Spitzer 24 μm band at $z \sim 2$. In most galaxies the primary emission mechanism at 8 μm is molecular band emission from aromatic "PAH" grain species, as distinct from the thermal grain emission that dominates in the FIR, so its reliability as a quantitative SFR tracer must be tested empirically. In massive galaxies with high SFRs the 8 μm emission correlates reasonably well with the TIR emission sufficiently so that it (or neighboring regions observed with the Infrared Space Observatory) has been calibrated as an IR SFR tracer of its own (e.g., Roussel et al. 2001, Boselli et al. 2004, Förster Schreiber et al. 2004, Wu al. 2005, Farrah et al. 2007, Zhu et al. 2008). However the dispersion in 8 μm luminosities at a fixed SFR tends to be higher than for longer wavelength tracers such as the 24 μm emission, with systematic dependences of the emissivity on metal abundance, and local radiation field strength and hardness (e.g., Madden 2000, Peeters et al. 2004, Engelbracht et al. 2005, 2008; Dale et al. 2005, Wu et al. 2006, Smith et al. 2007, C07). The large dispersion in PAH strength (more than an order of magnitude across all galaxy types and luminosities)

means that the rest 8 μm luminosity of a galaxy provides a crude measure at best of its SFR. Can these effects be mitigated by constructing a composite Hα + 8 μm SFR index?

To carry out this test we compiled 8 μm fluxes of the SINGS galaxies, both integrated fluxes and those with 20″ central apertures as described in §2. The emission in this bandpass is a composite of a (normally) dominant PAH band emission as well as an underlying continuum from dust and evolved stars. The pure dust emission at 8 μm was obtained by subtracting a scaled 3.6 μm emission from the measured 8 μm flux. A scale factor of 0.255 was used here, following C07. To provide a meaningful standard of comparison we also compiled MIPS 24 μm fluxes for the same objects. Stellar continuum in the 24 um band (apart from foreground stars, which were removed in the Dale et al. 2007 data) is negligible, so no attempt was made to remove it.

The top panels in Figure 15 show the correlation between 8 μm (left) and 24 μm luminosities and Balmer-corrected Hα luminosities for the sample of star-forming SINGS galaxies. Open circles show integrated measurements of the galaxies, while open squares show measurements of the central 20″ × 20″ star-forming regions. We have also overplotted in small dots the HII regions from the SINGS sample measured by C07.

The correlation between 24 μm and corrected Hα luminosities in the top right panel of Figure 15 is the same as seen earlier (Figure 6), but with a clear offset between the relations for entire galaxies and the HII regions, which we will return to later. The scatter in the relation between 8 μm emission and Hα emission is much higher, confirming trends seen in the HII regions by C07. Most of this difference reflects the presence of galaxies (and HII regions) with 8 μm luminosities up to 30 times weaker than the main relation; most of these are metal-poor dwarf galaxies, which are already known to have strongly suppressed PAH emission. The top left panel of Figure 15 aptly illustrates the perils of applying the 8 μm emission of galaxies indiscriminantly as a quantitative SFR tracer (cf. Smith et al. 2007, Engelbracht et al. 2008, and references therein).

The two bottom panels of Figure 15 show the results of constructing composite Hα + 8 μm and Hα + 24 μm estimates of the attenuation-corrected Hα luminosity, compared as before with the spectroscopically-corrected Hα luminosities. For the 24 μm index we used the same scaling factor a as for the integrated measurements earlier, to compare how well the central 20″ measurements and HII region measurements are fitted by the integrated relation. For the 8 μm + Hα composite we derived the value of $a = 0.011 \pm 0.001_{\rm r} \pm 0.003_{\rm s}$ (integrated and central 20″ data combined). For 24 μm the calibration from the SINGS and MK06 integrated measurements provides an excellent fit to the SINGS central aperture measurements as well, which is not surprising. What may be more surprising is the excellent consistency of the attenuation-corrected Hα luminosities derived from Hα + 8 μm with those

derived from the Balmer decrement attenuation corrections. The metal-poor outliers in the upper left panel of Figure 15 join the main relation in the weighted sum of Hα + 8 μm (lower left panel), because these galaxies have very low reddening and very low 8 μm emission, so both measured quantities in the plot are essentially (and identically) the observed Hα luminosity.

Interestingly the residuals using the 8 μm fluxes are lower than those derived using 24 μm fluxes, $\pm$0.11 dex vs $\pm$0.14 dex, respectively. This can be understood if the 8 μm luminosity is more tightly coupled to the TIR dust luminosities of galaxies than the 24 μm emission, as shown for example by Mattila et al. (1999), Haas et al. (2002), Boselli et al. (2004), and Bendo et al. (2008). Upcoming high angular resolution observations of the FIR continuum of the SINGS sample, currently planned with the *Herschel Space Observatory*, will allow us to test the coupling of the various IR emission components with higher spatial resolution and sensitivity.

5.2. Composite SFR Indices Using [O II] Emission Lines

In principle our approach can be applied to estimate dust attenuation corrections for any optical emission line that is used as a SFR diagnostic. The most commonly applied visible-wavelength line, especially for observations of galaxies at intermediate redshift, is the [O II]λ3727 forbidden line doublet. The chief advantage of this feature is that it is accessible to ground-based telescopes and CCD spectrometers out to redshifts $z \sim 1.7$, whereas Hα redshifts beyond the optical window above $z \sim 0.5$. As a result [O II]-based SFR estimates are available for tens of thousands of galaxies at $z \sim 0.1$–1.5 (e.g., Franzetti et al. 2007, Ly et al. 2007, Cooper et al. 2008).

The calibration and reliability of the [O II] feature as a quantitative SFR tracer has been discussed by several authors (e.g., Hopkins et al. 2003, Kewley et al. 2004, Moustakas et al. 2006). Unlike the Balmer lines, the luminosity of the collisionally-excited [O II] doublet is not fundamentally coupled to the ionizing flux, so its accuracy is limited by excitation variations, which in turn are systematically correlated with the metal abundance and ionization of the gas. However the typical variations in intrinsic [O II]/Hα are of order a factor of two or less over a wide range of abundances and galaxy environments, so the index can be useful, especially in applications to large samples. Dust attenuation however is a much more severe problem, with typical attenuations in normal galaxies of nearly an order of magnitude, and large variations between objects. Kewley et al. (2004) and Moustakas et al. (2006) provide empirical schemes for correcting for this attenuation as functions of [O II] luminosity and B-band luminosity, respectively, but these are crude approximations at best.

Here we investigate whether the combination of [O II] and IR luminosities can provide more robust attenuation-corrected SFRs.

Our results are summarized in Figure 16. The upper left panel compares the observed [O II] luminosities and reddening-corrected Hα luminosities for the MK06 sample (solid circles) and the inner $20'' \times 20''$ regions of the SINGS galaxies (open squares). The integrated measurements of the SINGS sample are not plotted because we do not have full-galaxy [O II] luminosities for that sample. This shows the worst case of applying the [O II] luminosity with no attenuation correction at all. By coincidence the mean attenuation-corrected luminosity of [O II] in the MK06 sample is nearly identical to that of Hα ($<$[O II]/H$\alpha>$ = 0.98), so any difference in luminosities translates identically to a deficit in the estimated SFR. On average the [O II] luminosities are suppressed by about 0.6 dex, with a range (excluding the two outliers) of 0.0–1.7 dex (a factor 50 at worst).

In the other three panels of Figure 16 we apply a weighted sum of [O II] luminosity and TIR, 24 μm, and 8 μm luminosities. As before we derived the coefficients a_λ from eq. (1) which best fit the mean relations in Figure 16. Combining observed [O II] luminosities of galaxies with any of the three IR luminosities can provide a credible attenuation correction to the [O II] luminosities, with dispersions that are comparable to their Hα + IR counterparts, when differences in sample are taken into account.

In §3.1 we pointed out that our linear combination method will be subject to modest systematic errors if the effective attenuation in the emission line of interest deviates significantly from the mean dust opacity of the stellar continuum radiation that heats the dust. In most normal galaxies the mean emission-line attenuation at [O II] is significantly higher than in the mean dust-heating stellar continuum (Calzetti 2001), so we might expect our residuals to show a mild dependence on attenuation, as illustrated theoretically in Figure 3. We examined the residuals for such an effect, and observe a qualitative trend in the expected sense, but we cannot reliably separate this from trends introduced by systematic variations in the intrinsic strength of [O II] relative to the Balmer lines. However there is other evidence for this effect from the fact that the best fitting values of a in Figure 16 are about 40%–50% higher than the corresponding values for Hα, even though the intrinsic luminosities of [O II] and Hα are nearly identical. This difference in fitting coefficients (see Table 4) is a direct result of the higher dust attenuation at [O II].

5.3. Composite SFRs Using Radio Continuum Emission

All of the composite SFR methods described until now require flux measurements in at least one IR band. It is well known that star-forming galaxies show a tight, linear correlation between their FIR and radio continuum luminosities (e.g., Condon et al. 1991, Yun et al. 2001), so it should be possible to use the radio continuum emission in combination with optical and UV star formation tracers to derive attenuation-corrected SFRs. In this section we extend our tests to 1.4 GHz radio continuum fluxes, to evaluate the reliability of such hybrid SFR measures.

The results of our comparison are shown in Figure 17. The top panel shows the relationship between observed 1.4 GHz (21 cm) radio continuum luminosity and Balmer-corrected Hα luminosity, while the bottom panel shows the correlation between a weighted sum of uncorrected Hα and radio luminosity with the same Balmer-corrected Hα luminosities luminosities. These can be compared directly to Figures 6 and 7, which shows similar comparisons but with 24 μm and TIR luminosities, respectively. Qualitatively the radio continuum fluxes and composite SFR indices show that same behavior as we found for their IR counterparts. The 1.4 GHz radio luminosities by themselves show a nonlinear dependence on the attenuation-corrected Hα luminosities (Bell 2003), with a power-law slope of 1.28, even steeper than that seen in TIR luminosity (1.10) and 24 μm luminosity (1.19). However combining the Hα and radio luminosities removes most of the nonlinearity and much of the dispersion, confirming that the radio luminosities can be used to correct the optical lines for attenuation as well. The mean dispersions around the fits ($\pm$0.10 dex for Hα + 1.4 GHz and $\pm$0.12 dex for [O II] + 1.4 GHz) are 11%–33% larger than the corresponding Hα + TIR and [O II] + TIR indices, but again these dispersions are small when compared to the random and systematic errors in SFRs derived from any of the individual SFR tracers by themselves.

It is interesting that the sense of the nonlinearity in the radio–FIR relation is in the opposite sense that one might naively expect. At 1.4 GHz the radio continuum is dominated by non-thermal (synchrotron) emission, which presumably originates ultimately from supernova events; this interpretation forms the physical basis for using the non-thermal radio emission as a SFR tracer (e.g., Condon 1992 and references therein). If this scaling of radio continuum luminosity with the SFR strictly held over all types and luminosities of star-forming galaxies, then one would expect the correlation in the upper panel of Figure 17 to be strictly linear, while the slope of the radio vs TIR correlation shown in Figure 18 would be considerably shallower than a linear relation, because we already have seen that the dust emission systematically underestimates the SFR in low-luminosity, low-opacity galaxies. Instead Figure 17 shows a nonlinear dependence of radio emission on attenuation-corrected SFR (also see Bell 2003), and the slope of the radio vs TIR correlation in Figure 18 is *steeper* than a

linear relation. Apparently the radio emissivity of galaxies declines even more steeply at low luminosity than even the dust emission, producing the residual nonlinearities in Figure 17 and 18. A discussion of the physical explanation for this result is beyond the scope of this paper. One possibility is a systematic change in the cosmic ray lifetimes and/or the magnetic field strengths of galaxies with changing mass and SFR. Another possibility is the increasing role of radio emission from a nuclear accretion disk in more massive galaxies. Whatever the explanation, our results demonstrate that the radio continuum luminosities of galaxies can be combined with emission-line luminosities to provide reasonable measurements of the attenuation-corrected SFRs.

6. Discussion: Recommendations and Limitations

The results of §4 and §5 are very encouraging in demonstrating that linear combinations of optical emission-line luminosities with a number of IR and radio continuum luminosities can be used to produce attenuation-corrected luminosities and SFRs. In Table 4 we summarize the best fitting coefficients a (equations [1] and [2]) for each combination of optical and IR or radio continuum indices, along with its formal uncertainty, and the mean dispersion of individual galaxy luminosities around the best fitting relation. For completeness we also list the corresponding values for the SINGS and MK06 samples measured separately.

Among the many alternatives, the combination of Hα and TIR luminosities offers the most robust attenuation corrections, with a precision that rivals or exceeds that obtainable from de-reddening high quality integrated optical spectra, and the weakest systematic dependences on the SEDs and star formation properties of the parent galaxies. However for many applications reliable wavelength-integrated TIR luminosities are not available, and in such situations single-band measurements of the rest-frame 24 μm or 8 μm infrared fluxes, or alternatively the 1.4 GHz radio continuum fluxes appear to perform nearly as well as combinations using the TIR fluxes.

6.1. Composite Multi-wavelength SFR Calibrations and Extinction Estimates

Throughout this analysis we have compared the different SFR tracers referenced to the total attenuation-corrected Hα luminosity, rather than the SFR itself. We chose this convention to anchor our results firmly in terms of observable quantities, and to circumvent the additional systematic effects that enter into the conversion of Hα luminosities into SFRs. However one can readily use the coefficients listed in Table 4 to construct SFR calibrations

using these composite indicators. Apart from their dependence on the coefficients in Table 4, these absolute SFR calibrations also scale with the zero-point of the reference SFR vs L(Hα) calibration. The latter is dependent on the assumed slope and mass limits of the IMF, and on the stellar synthesis models used in deriving this calibration. For convenience we provide two such calibrations, one on the zero-point of the widely-applied calibration of K98, and the other using a more realistic "Kroupa" IMF (Kroupa & Weidner 2003), as used in the current version of the Starburst99 synthesis models (Leitherer et al. 1999).

The calibration of K98 assumed for simplicity a single Salpeter (1955) slope power-law, with $\xi(m) \propto m^{-\alpha}$ with $\alpha = 2.35$ between 0.1–100 $M_\odot$, where $\xi(m) \equiv dN/dm$ is the number of stars with masses between m and $m + dm$. Ionizing luminosities for that calibration were taken from Kennicutt et al. (1994). For this zero-point the composite SFR calibrations take the form:

$$\mathrm{SFR[K98]}(M_\odot\, yr^{-1}) = 7.9 \times 10^{-42}[L(H\alpha)_{obs} + a_\lambda\, L_\lambda]\ (\mathrm{ergs\,s^{-1}}), \tag{11}$$

where L(Hα)$_{obs}$ is the observed Hα luminosity without correction for internal dust attenuation, a_λ is taken from Table 4 for the IR or radio luminosity of interest (8 μm, 24 um, TIR, or 1.4 GHz), and L_λ is the luminosity in the respective wavelength band. As an example, the calibration for the combination of Hα and 24 μm luminosities is:

$$\mathrm{SFR[K98]}(M_\odot\, yr^{-1}) = 7.9 \times 10^{-42}[L(H\alpha)_{obs} + 0.020L(24)]\ (\mathrm{ergs\,s^{-1}}), \tag{12}$$

where $L(24) \equiv \lambda\, \mathrm{L}_\lambda$ at 24 um (or 25 μm). For this example the dust attenuation at Hα would be given by:

$$\mathrm{A(H\alpha)(mag)} = 2.5 \log [1 + \frac{0.020\, L(24)}{L(H\alpha)_{obs}}] \tag{13}$$

The analogous calibration for indices using measurements of the [O II]λ3727 doublet is:

$$\mathrm{SFR[K98]}(M_\odot\, yr^{-1}) = 8.1 \times 10^{-42}[L([\mathrm{OII}])_{obs} + a'_\lambda\, L_\lambda]\ (\mathrm{ergs\,s^{-1}}). \tag{14}$$

Here we have designated the scaling coefficients a'_λ with a prime symbol to emphasize that these coefficients are different from those derived for Hα. Again, as an example, the corresponding calibration for combining [O II] and 24 μm luminosities is:

$$\mathrm{SFR[K98]}(M_\odot\, yr^{-1}) = 8.1 \times 10^{-42}[L([\mathrm{OII}])_{obs} + 0.029L(24)]\ (\mathrm{ergs\,s^{-1}}), \tag{15}$$

The second IMF, which we refer to for convenience as a "Kroupa" IMF, has the slope $\alpha = 2.3$ for stellar masses 0.5–100 $M_\odot$, and a shallower slope $\alpha = 1.3$ for the mass range 0.1–0.5 $M_\odot$. The Kroupa IMF is more consistent with recent observations of the Galactic field IMF (e.g., Chabrier 2003, Kroupa & Weidner 2003). We also have recalibrated the ionization rate from this stellar population using Version 5.1 of Starburst99[5]. For these models the zero-point of the SFR is lower than for the K98 calibration by a factor of 1.44. As a result the calibrations in eqs. (11) and (14) become:

$$\mathrm{SFR[Kroupa]}(M_\odot\, yr^{-1}) = 5.5 \times 10^{-42}[L(H\alpha)_{obs} + a_\lambda\, L_\lambda]\ (\mathrm{ergs\,s^{-1}}), \tag{16}$$

$$\mathrm{SFR[Kroupa]}(M_\odot\, yr^{-1}) = 5.6 \times 10^{-42}[L([\mathrm{OII}])_{obs} + a'_\lambda\, L_\lambda]\ (\mathrm{ergs\,s^{-1}}), \tag{17}$$

6.2. Applicability Limits: Where Do These Methods Break Down?

As with any empirical "toolbox" of SFR calibrations, these composite indicators have been calibrated over limited ranges of galaxy properties, SFRs, and physical environments, and it is important to understand both the range of observations beyond which the methods are untested, and any systematic errors that may have been built into the zero-points of the methods. We refer readers to the review in K98 for a discussion of the assumptions and systematic uncertainties underlying the individual SFR tracers that have been considered in this paper. However there are a few additional cautions and caveats that apply to this new set of composite indicators.

The parent SINGS and MK06 galaxy samples cover essentially the full range of galaxy types found in the local universe, ranging from virtually dust-free dwarf galaxies to ULIRGs and luminous AGN hosts. However we needed to restrict our analysis to star-forming galaxies with high signal/noise multi-wavelength data, and this vetting process narrowed the coverage of galaxy properties covered by these calibrations. In particular our galaxies cover restricted ranges in Hα attenuation (0 – 2.5 mag) and corresponding observed $L(TIR)/L(H\alpha)$ ratio (45 – 3150), as well as in underlying stellar population and age ($D_n(4000) \leq 1.4$), corresponding roughly to the transition between lenticular (S0) and spiral galaxies. The highest IR luminosities in our final sample were $\log L(TIR)/L_\odot \sim 11.9$, just below the threshold for a ULIRG, and the highest attenuation-corrected SFRs are $\sim$100 $M_\odot\,\mathrm{yr}^{-1}$. This range readily encompasses all normal galaxies in the present-day universe and most star-forming galaxies

[5]URL: http://www.stsci.edu/science/starburst99/

out to redshifts $z \sim 1$. However it does not encompass the most luminous star-forming galaxies found at high-redshift, or the most dust-obscured LIRGs or ULIRGs found in the present-day universe. At the other extreme, our methods can break down for early-type red galaxies with very low SFRs, where the dominant IR dust emission can arise from evolved stars (e.g., Cortese et al. 2008, Johnson et al. 2009). Both red dusty galaxies and very dusty starburst galaxies will manifest themselves by very red colors in the visible and/or by anomalously large $L(IR)/L(H\alpha)$ ratios, and application of the limits above can flag such potentially problematic cases. We still believe that these composite methods provide more robust SFRs than any of the single-wavelength methods, but one should attach larger systematic errors (up to a factor of two) for systems that lie outside of the bounds of our calibrations.

As an additional cautionary note, we emphasize that the relations in Table 4 were derived from integrated measurements of entire galaxies, or of regions covering several square kiloparsecs in area in the centers of galaxies, and as such the SFR calibrations given here only apply in regions that encompass a representative sampling of the integrated light of a galaxy. In particular, the coefficients a differ significantly from those of individual HII regions and HII region complexes. When we compare the relation between Hα and 24 μm luminosities of SINGS HII regions (C07) with that for the integrated measurements of galaxies, we observe a significant offset (see Figure 15), with a best fitting value $a_{24} = 0.031 \pm 0.006$ for the HII regions, compared to $a_{24} = 0.020 \pm 0.001_{\rm r} \pm 0.005_{\rm s}$ for the galaxies. This difference is almost certainly due to the different stellar age distributions in the HII regions and the galaxies as a whole. The ionizing lifetimes of O-stars are nearly all less than 5 Myr, so in HII regions the massive early-type stars dominate both the gas ionization and the heating of the dust that produces the 24 μm dust emission. On the other hand when one measures entire galaxies that ionized gas emission is still dominated by massive O-stars, but the dust heating includes an additional component from stars older than 5 Myr.

We can estimate the importance of this change in stellar populations quantitatively, by comparing the evolution in ionizing UV, far-UV, and bolometric luminosities of star-forming populations with age. We used Version 5.1 of the Starburst99 package of Leitherer et al. (1999) to trace the evolution of Hα luminosity, 1500 Å UV continuum luminosity, and bolometric luminosity for continuously star-forming populations with ages of 5 Myr (appropriate to an HII region), and 0.1–1 Gyr (appropriate for galaxies, the ratios do not change significantly at larger ages). For either a Salpeter or Kroupa IMF as defined in §6.1 the ratio of bolometric luminosity to Hα luminosity increases by a factor of ∼2.0 between ages of 5 Myr and 100 Myr (and ∼2.5 when compared to age 1 Gyr). We expect the ratio of dust luminosity to ionizing luminosity to be less sensitive to these age differences, however, because the attenuation of a given population decreases with increasing stellar age (e.g., Zaritsky et

al. 2002). If we apply the prescriptions of Charlot & Fall (2000) or Calzetti et al. (2000), we expect the HII regions to experience ∼2–3 times the dust attenuation as the average starlight in a starburst population. Thus the additional component of UV/bolometric luminosity in an older population should increase the dust emission (for a given fixed ionizing luminosity) by a factor 1.4–1.6, similar to the difference in 24 μm/Hα ratios we observe between the HII regions and the galaxies.

This "older" dust emission component can be directly observed in our *Spitzer* 24 μm images of the SINGS galaxies. Figure 19 compares 24 μm and Hα images of M81, a nearby, well-resolved spiral galaxy that clearly illustrates the different IR emission components. Virtually all of the 24 μm point sources are associated with bright optical HII regions (Prescott et al. 2007), which validates our association of the 24 μm emission with the dust attenuation in the HII regions. However upon closer examination a diffuse IR emission component can also be observed, which extends between the HII regions and exhibits a more filamentary morphology, roughly tracing that of the HI gas and the diffuse 8 μm PAH emission (e.g., Gordon et al. 2004; Pérez-González et al. 2006). This diffuse component is the "infrared cirrus" component of the dust emission and has been identified in many other galaxies observed with *ISO* and *Spitzer* (e.g., Hippelein et al. 2003; Hinz et al. 2004; Popescu et al. 2005). According to the measurements of Dale et al. (2007) this diffuse component contributes ∼50% of the total 24 μm emission in M81, similar to the average fraction in the SINGS sample as a whole. These observations tend to support the suggestion by Zhu et al. (2008) that the difference in the 24 μm vs Hα correlations between galaxies and HII regions are due to the presence of diffuse IR emission.

These results should serve as a stern warning that the composite SFR indicators calibrated in this paper, C07, and Zhu et al. (2008) *cannot be applied to map the spatially-resolved SFR in galaxies* without the risk of introducing significant and possibly large systematic errors in the resulting SFR maps. Our results show that these methods can be applied reliably to individual HII regions and to galaxies as a whole (albeit with different scaling factors between optical and IR emission). However when observed at high spatial resolution galaxies show diffuse components of both Hα and IR emission which may be completely unassociated with any star formation at the same position. The diffuse IR component is especially problematic, because this dust may be only partially heated by young stars, or possibly not by young stars at all. As a result blind application of the relations in Table 4 to multi-wavelength images of galaxies will tend to produce large regions with spuriously high "SFRs" where little or no star formation actually is taking place. Methods incorporating other information will be needed to extend this type of analysis to make reliable spatially-resolved maps of star formation in galaxies.

6.3. Systematic Uncertainties

We conclude by re-examining the possibility of systematic errors in our attenuation scales (§3.3), now informed by the results presented in the previous sections. The most important assumptions are the adoption of reference attenuation corrections based on Balmer decrements with a Galactic extinction curve and a foreground screen dust geometry, and the assumption of a constant intrinsic ratio of ionizing luminosity to bolometric luminosity.

One of the surprises in the results (to us), has been the relatively tightness of the relations between the attenuation-corrected Hα luminosities, surface brightnesses, and attenuations themselves derived from linear combinations of Hα and IR (or radio) luminosities, when compared to the same corrected quantities derived from Balmer decrement measurements. The agreement in the mean attenuations is not significant at all, of course, because we calibrated the scales to match, but the relatively low dispersions in the comparisons shown in Figures 6–13, along with the absence of significant nonlinearities suggests that any systematic effects from variations in dust geometry and stellar population variations are likely to be of secondary importance.

Although the consistency of our results is encouraging, it does not rule out the possibility of a systematic error that affects the entire attenuation and SFR scales, or a systematic error that scales smoothly with the SFR itself. Perhaps the most vulnerable assumption is the adoption of the stellar-absorption corrected Balmer decrement in the integrated spectrum (using a foreground dust screen approximation) as the reference for calibrating our composite SFR and attenuation scales. Galaxies clearly display point-to-point variations in line-of-sight attenuation, with the integrated spectrum representing a flux-weighted average, including effects of scattered light. Although recent models suggest that the foreground dust screen approximation does not introduce significant systematic errors when applied to normal star-forming galaxies (Jonsson et al. 2009), it is important to place limits on the magnitude of any systematic errors in our calibrations and attenuation scales resulting from these simplifying assumptions.

Ideally one would use as references measurements of ionizing fluxes of galaxies that are less susceptible to dust attenuation, such as the Paschen or Brackett emission lines, or the free-free thermal radio continuum, which scales directly with the ionizing flux. Unfortunately such measurements are not available for large samples of galaxies, or contain such large uncertainties that they cannot be applied individually to galaxies. That is why we have chosen to base our analysis on Balmer decrement measurements. However some of these measurements are available for subsets of our sample, and we can use these to estimate Hα attenuations and compare them to those we derived from the Balmer decrements.

Our first empirical test comes from Pa α and Hα measurements for 29 of the SINGS galaxies in our sample (C07). The Pa α observations were made with the Near-Infrared Camera and Multi-Object Spectrometer (NICMOS) on the Hubble Space Telescope, and are restricted to the central $50'' \times 50''$ regions of the galaxies (and a $144''$ field for M51). We used the Pa α fluxes to derive attenuation-corrected Hα luminosities, using the theoretical recombination ratio as described in C07, and using the observed ratio of Pa α/Hα fluxes to correct for the (weak) attenuation in Pa α ($\lambda = 1.89\,\mu$m). We do not have optical spectra with matching coverage to these regions, but we can measure Hα and $24\,\mu$m fluxes over the same regions, and derive attenuation-corrected Hα luminosities, using eq. (1) with $a = 0.020$, as calibrated from our Balmer decrement measurements. Figure 20 compares the resulting Hα surface brightnesses (cf. Figure 9) using the two methods. There is a considerable scatter in the comparison, which probably reflects the measuring uncertainties in the Paα photometry. The two scales are in good agreement, with an average difference of 0.024±0.036 dex (attenuation from Pa α/Hα higher by 0.06±0.09 mag) and no evidence for nonlinearity, over a full range of 3 mag in A(Hα).

Estimated thermal fractions of radio continuum fluxes are available for 27 galaxies in our sample from the study of Niklas et al. (1997). The thermal radio component arises from free-free emission of thermal electrons in the ionized gas, and its brightness scales directly with the unattenuated Hα emission, with a weak dependence on electron temperature (Niklas et al. 1997):

$$S_{th}(mJy) = (\frac{2.24 \times 10^9\, S_{H\alpha}}{ergs\, s^{-1}\, cm^{-2}})(\frac{T_e}{K})^{0.42}(\ln(\frac{0.05}{\nu/GHz}) + 1.5\, \ln(T_e/K)). \quad (18)$$

Since the dust extinction in the radio is negligible the ratio of thermal radio to Hα flux provides a measure of the Hα attenuation that is unaffected by any geometric effects in the Balmer extinction. For most galaxies the thermal component of the radio emission represents only a small fraction of the total emission at centimeter wavelengths, with the dominant contribution arising from non-thermal synchrotron emission. Niklas et al. (1997) obtained integrated radio fluxes at several (typically 6–7) wavelengths, in order to decompose the thermal and non-thermal components. The resulting thermal radio fractions and fluxes for individual galaxies have an average uncertainties of ±0.33 dex (0.83 mag), but this is sufficient to test for a systematic difference in Hα flux scales. Figure 21 shows a histogram of the differences between the Hα attenuations estimated from the radio/Hα ratios using eq. (18) under the assumption of $T_e = 10^4 K$, and those derived from the Hα/Hβ ratios. The median radio continuum attenuation (more reliable than the mean given the large scatter in measurements) is 0.02 ± 0.13 mag lower than that estimated from the Balmer decrements. In view of the large uncertainty in the radio measurements we cannot rule out a small systematic

bias in the Balmer decrement measurements, but this test, as with the Pa α measurements, appears to rule out a significant systematic error.

For our final empirical test we compared the attenuations estimated from the Balmer decrements with those which can be derived by comparing the resulting Hα-based SFRs with attenuation-corrected SFRs from UV and IR measurements. This test is less direct than those based on radio continuum and Pa α measurements described above, because the intrinsic ratio of Hα and UV continuum luminosities of a galaxy are dependent on other factors including the star formation history and the slope and upper mass limit of the IMF. We address this in detail in Paper II, but apply a simple test here to place limits on any systematic errors in the Balmer decrement based attenuation measurements.

Several authors have published prescriptions for using the combination of UV and IR fluxes of galaxies to derive attenuation-corrected UV luminosities and SFRs, based on energy-balance arguments that are similar to those presented in this paper (e.g., Gordon et al. 2000; Bell 2003; Hirashita et al. 2003; Kong et al. 2004; Buat et al. 2005; Iglesias-Páramo et al. 2006; Cortese et al. 2008). We have applied the prescriptions of Kong et al. (2004) and Buat et al. (2005), which lie in the mid-range of published calibrations, to FUV and TIR luminosities of the SINGS and MK06 galaxies (Paper II), to derive attenuated-corrected FUV luminosities, and converted these to SFRs using the most recent Starburst99 models and the Kroupa IMF described in §6.1. These yield:

$$SFR(M_{\odot}\,yr^{-1}) = 8.8 \times 10^{-29} L_{\nu}(ergs\,s^{-1}\,Hz^{-1}) \tag{19}$$

We then compared these SFRs to those derived from the observed (uncorrected) Hα luminosities, for the same synthesis models and IMF:

$$SFR(M_{\odot}\,yr^{-1}) = 5.5 \times 10^{-42} L(H\alpha)(ergs\,s^{-1}) \tag{20}$$

The ratio of the attenuated-corrected FUV-based SFR to the uncorrected Hα-based SFR provides an indirect estimate of the attenuation in Hα. We find that these attenuation estimates are slightly higher than those derived from the Balmer decrements in the foreground screen approximation, by 0.08 mag in the median for the Kong et al. (2004) calibration and by 0.18 mag for the Buat et al. (2005) calibration. Since the average Hα extinction for the sample is 0.8 mag, the UV-based attenuation estimates are higher by 10% and 23% respectively. Our own calibration in Paper II (which do not depend explicitly on the Balmer attenuation scale) yields attenuations that are close to those derived by Kong et al. (2004). As a check, one can also use the UV and IR fluxes to derive the FUV attenuation directly

using the published calibrations by those authors, and apply the Calzetti (2001) attenuation law to estimate $A_{H\alpha}$ from A_{FUV}. This yields Hα attenuations which are 0.10, 0.15, and 0.07 mag higher than the Balmer-derived attenuations, for the calibrations of Kong et al. (2004), Buat et al. (2005), and Paper II, respectively. These are very close to the values derived from a comparison of FUV and Hα-based SFRs above. Based on the dependence of these results on the calibration used, as well as the systematic dependences on stellar age mix and IMF we conservatively estimate in the uncertainties in the comparison of UV+IR and Balmer-line attenuation estimates to be $\pm$20%. Therefore if we average the results based on Kong et al. (2004) and Buat et al. (2005) we find a difference in attenuations of 0.13 ± 0.16 mag.

Taken together, the Paα, thermal radio continuum, and UV+IR based estimates of Hα attenuations give average values that are 0.06 $\pm$ 0.09 mag higher, 0.02 $\pm$ 0.13 mag lower, and 0.13 $\pm$0.16 mag higher than those derived from the Balmer decrements. This may hint at a slight tendency for the Balmer decrements to under-estimate the actual Hα attenuations, but within the uncertainties the scales are consistent. It is also notable that other widely adopted schemes such as the modified Charlot-Fall attenuation law (Wild et al. 2007; da Cunha et al. 2008) produce attenuations that are within 0.1 mag on average of those derived here. These results rule out large systematic errors in our attenuation scale, with a very conservative upper limit of 20%.

The other important assumption underlying our analysis is the implicit adoption of a constant dust-heating stellar population for all of the galaxies in our sample. This is the same "IR cirrus" problem that has bedeviled efforts to calibrate the IR emission of galaxies as a quantitative SFR tracer (e.g., Lonsdale Persson & Helou 1987, Sauvage & Thuan 1992). We already have seen evidence for the effects of varying stellar population in the comparison of calibrations of eq. (1) between disk HII regions and integrated measurements of galaxies (§6.2). The results suggest that although the coefficients a derived in this paper appear to apply over a wide range of normal galaxy populations, they may systematically under-estimate the SFR by as much as 60% in systems that are dominated by young stars, such as emission-line starburst galaxies and possibly luminous and ultraluminous starburst galaxies with young dust-heating stellar populations.

This difference in calibrations helps to account for a curious inconsistency between our results and previous calibrations of SFRs for starbursts by K98 and other authors. The relationship from that paper:

$$SFR(M_{\odot}\, yr^{-1}) = 4.5 \times 10^{-44} L_{bol}(ergs\, s^{-1}) \tag{21}$$

yields SFRs that can be up to 2.2 times higher than those given by eq. (11) and the

coefficients in Table 4, when applied to very dusty galaxies, where the TIR term in eq. (11) dominates. Most of this difference can be readily accounted for by the different assumptions underlying the two calibrations. The K98 relation is entirely theoretical, and it assumes dust heating by stars with ages less than 30 Myr, whereas the relations in this paper were calibrated empirically, and automatically incorporate any contributions to dust heating from stars older than 30 Myr. If one adopts instead a bolometric based SFR calibration using a dust-heating continuum that is appropriate for normal spiral galaxies (continuous star formation over 1–10 Gyr) the inconsistencies with the empirical calibrations in this paper largely disappear. Taken at face value this would suggest that approximately half of the dust heating in the galaxies in our sample arises from stars older than 30 Myr (Cortese et al. 2008; Johnson et al. 2009).

To investigate this quantitatively we have applied the simple dust radiative transfer model of C07 to calculate approximately the expected TIR emission from a disk galaxy with a constant star formation history over the past 10 Gyr. The C07 models were parameterized in terms of the SFR per unit area, and we converted these approximately to luminosities by using the median area of the Hα disks of the SINGS galaxies (200 kpc^2). The model relation is plotted with the observations in the right panel of Figure 22, for the fitted value $a = 0.0024$, while the left panel shows for comparison the expected relation if only stars younger than 30 Myr heated the dust. The consistency of the model with the fitted attenuation corrections suggests that any bias in the SFR scales from systematic errors in the Balmer-based attenuation corrections is small.

Our focus on possible systematic effects should not obscure the immense improvements in the reliability of SFRs that are afforded by these composite tracers. Many current measurements of SFRs are based on observations at a single wavelength region, with perhaps a crude statistical correction for dust attenuation. As shown in the upper panels of Figures 6–8, the random uncertainties in SFRs produced by these single-tracer methods is typically of order a factor of two, and systematic errors can easily reach a factor of ten or higher. The methods developed here reduce the random errors in the attenuation corrections from factors of a few to of order ±15–30%, and systematic errors to of order ±10% in most galaxies. As discussed above systematic errors of up to a factor of two may be present in the worst cases, but those errors are due to uncertainties in stellar populations in the galaxies, *not* in the dust attenuation scales. Other factors such as IMF variations may introduce larger errors in the SFR scales than discussed here, but at least one should be able to remove dust attenuation as the dominant source of uncertainty in the extragalactic SFR scale.

7. Summary

We have used two samples of galaxies with measurements of the optical emission lines and infrared and radio continuum to explore the combination of optical and IR (or radio) fluxes to derive attenuation-corrected SFRs. Our main conclusions can be summarized as follows.

1. Linear combinations of Hα and total infrared (TIR) luminosities provide estimates of Hα attenuation (and thus attenuation-corrected Hα luminosities) that are in good agreement with those derived from measurements of the stellar absorption-corrected Hα/Hβ ratios (Balmer decrements). The corrected luminosities agree to within $\pm$23% rms, with essentially no systematic dependence on luminosity, surface brightness, or spectral properties of the stellar population, over the range of galaxy types, and SFRs tested.

2. Similar linear combinations of Hα luminosities with single-band IR luminosities (e.g., 24 μm, 8 μm) provide attenuation corrections that are nearby as consistent with Balmer decrement measurements as those derived from combinations of Hα and TIR measurements. Combinations of Hα and 24 μm measurements show small systematic variations which correlate with IR SED shape, and can be understood as correlating with the fraction of dust luminosity that is radiated in the 24 μm band.

3. The same methodology can be applied to other optical emission-line tracers (e.g., [O II]λ3727) or using the 1.4 GHz radio continuum emission in lieu of infrared continuum measurements.

4. For a given attenuation in the Hα line the ratio of IR/Hα luminosities is systematically higher for integrated measurements of galaxies than it is for individual HII regions or star-forming complexes. We attribute most or all of this effect to differences in the mean ages of the stars heating the dust in galaxies and HII regions. This excess dust heating from a non-star-forming population is in good agreement with expectations from evolutionary synthesis models.

5. A corollary conclusion of the previous result is that a considerable fraction of the total infrared radiation in normal star-forming galaxies is heated by stars older than 100 Myr. Comparisons with evolutionary synthesis models suggests that up to 50% of the TIR emission could be from dust heated from this evolved stellar population. Part of this excess emission is probably associated with the diffuse "infrared cirrus" dust emission in galaxies, but not necessarily uniquely associated, because it is possible that young stars may also partially heat the diffuse dust.

6. We present prescriptions for measuring SFRs of galaxies from linear combinations of

Hα or [O II]λ3727 emission lines with TIR, 24 μm, or 8 μm infrared measurements, or 1.4 GHz radio continuum measurements. These appear to be reliable for normal star-forming galaxies with SFRs in the range 0–80 $M_\odot\,yr^{-1}$ and A(Hα) = 0 – 2.5 mag. The calibrations may be less reliable for early-type galaxies with UV–optical radiation fields dominated by evolved stars, or for very highly obscured starburst galaxies, where very young stars dominate dust heating.

7. We carefully examine the systematic reliability of our SFR scales. The use of Balmer line ratios from optical spectra to anchor the attenuation scale may introduce a small systematic bias in the SFR scales, but comparisons to independent tracers show that these errors are probably less than 15% on average. Variations in dust heating stellar populations in galaxies are probably a larger source of systematic error. In particular our prescriptions yield SFRs for dusty IR-luminous starburst galaxies that are approximately a factor of two lower than those given by the widely used calibration in Kennicutt (1998a), possibly due to an inapplicability of our algorithms in this extreme star formation regime. Overall we expect that these algorithms should provide attenuation-corrected SFRs accurate to $\pm$0.3 dex or better for nearly all star-forming galaxies, excluding possible effects of variable IMFs.

This work is based in part on observations made with the Spitzer Space Telescope, which is operated by the Jet Propulsion Laboratory, California Institute of Technology, under a contract with NASA. Support for this work was provided by NASA through an award issued by JPL/Caltech. C. Hao gratefully acknowledges the support of a Royal Society UK–China Fellowship. C. Hao also acknowledges the support from NSFC key project 10833006. We also gratefully acknowledge a critical reading of the paper by an anonymous referee, who led us to undertake a much more rigorous analysis of the systematic uncertainties in our methods.

REFERENCES

Adelman-McCarthy, J. K., et al. 2006, ApJS, 162, 38

Alonso-Herrero, A., Rieke, G.H., Rieke, M.J., Colina, L., Pérez-González, P.G., & Ryder, S.D. 2006, ApJ, 650, 835

Balogh, M. L., Morris, S. L., Yee, H. K. C., Carlberg, R. G., & Ellingson, E. 1999, ApJ, 527, 54

Bavouzet, N., Dole, H., Le Floc'h, E., Caputi, K. I., Lagache, G., & Kochanek, C. S. 2008, A&A, 479, 83

Bell, E.F. 2003, ApJ, 586, 794

Bendo, G. J., et al. 2008, MNRAS, 389, 629

Boselli, A., Lequeux, J., & Gavazzi, G. 2004, A&A, 428, 409

Bresolin, F., Kennicutt, R. C., & Garnett, D. R. 1999, ApJ, 510, 104

Brinchmann, J., Charlot, S., White, S. D. M., Tremonti, C., Kauffmann, G., Heckman, T., & Brinkmann, J. 2004, MNRAS, 351, 1151

Bruzual, G. 1983, ApJ, 273, 106

Buat, V., et al. 2005, ApJ, 619, L51

Calzetti, D. 2001, PASP, 113, 1449

Calzetti, D., Arums, L., Bohlin, R.C., Kinney, A.L., Koorneef, J., & Storchi-Bergmann, T. 2000, ApJ, 533, 682

Calzetti, D., Kinney, A.L., & Storchi-Bergmann, T. 1994, ApJ, 429, 582

Calzetti, D., et al. 2005, ApJ, 633, 871

Calzetti, D., et al. 2007, ApJ, 666, 870 (C07)

Caplan, J., & Deharveng, L. 1986,A&A, 155, 297

Chabrier, G. 2003, PASP, 115, 763

Charlot, S., & Fall, S.M. 2000, ApJ, 539, 718

Charlot, S., & Longhetti, M. 2001, 323, 887

Condon, J.J. 1987, ApJS, 65, 485

Condon, J.J. 1992, ARA&A, 30, 575

Condon, J. J., Anderson, M. L., & Helou, G. 1991, ApJ, 376, 95

Condon, J. J., Cotton, W. D., Greisen, E. W., Yin, Q. F., Perley, R. A., Taylor, G. B., & Broderick, J. J. 1998, AJ, 115, 1693

Cooper, M.C., et al. 2008, MNRAS, 383, 1058

Cortese, L., Boselli, A., Franzetti, P., Decarli, R., Gavazzi, G., Boissier, S., & Buat, V. 2008, MNRAS, 386, 1157

da Cunha, E., Charlot, S., & Elbaz, D. 2008, MNRAS, 388, 1595

Dale, D. A., & Helou, G. 2002, ApJ, 576, 159

Dale, D. A., et al. 2005, ApJ, 633, 857

Dale, D. A., et al. 2007, ApJ, 655, 863

de Vaucouleurs, G., de Vaucouleurs, A., Corwin, H.G., Buta, R.J., Paturel, G., & Fouque, P. 1991, Third Reference Catalog of Bright Galaxies, Berlin: Springer (RC3)

Engelbracht, C.W., Gordon, K. D., Rieke, G. H., Werner, M. W., Dale, D. A., & Latter, W. B. 2005, ApJ, 628, L25

Engelbracht, C. W., Rieke, G. H., Gordon, K. D., Smith, J.-D. T., Werner, M. W., Moustakas, J., Willmer, C. N. A., & Vanzi, L. 2008, ApJ, 678, 804

Farrah, D., et al. 2007, ApJ, 667, 149

Ferguson, A. M. N., Gallagher, J. S., & Wyse, R. F. G. 1998, AJ, 116, 673

Förster Schreiber, N.M., Roussel, H., Sauvage, M., & Charmandaris, V. 2004, A&A, 419, 501

Franzetti, P., et al. 2007, A&A, 465, 711

Garnett, D. R., & Shields, G. A. 1987, ApJ, 317, 82

Garnett, D. R., Shields, G. A., Peimbert, M., Torres-Peimbert, S., Skillman, E. D., Dufour, R. J., Terlevich, E., & Terlevich, R. J. 1999, ApJ, 513, 168

Garnett, D. R., Shields, G. A., Skillman, E. D., Sagan, S. P., & Dufour, R. J. 1997, ApJ, 489, 63

Gordon, K.D., Clayton, G.C., Witt, A.N., & Misselt, K.A. 2000, ApJ, 533, 236

Gordon, K.D. et al. 2004, ApJS, 154, 215

Haas, M., Klaas, U., & Bianchi, S. 2002, A&A, 385, L23

Hawley, S. A., & Phillips, M. M. 1980, ApJ, 235, 783

Hinz, J. L., et al. 2004, ApJS, 154, 259

Hippelein, H., Haas, M., Tuffs, R. J., Lemke, D., Stickel, M., Klaas, U., & Volk, H. J. 2003, A&A, 407, 137

Hirashita, H., Inoue, A. K., Kamaya, H., & Shibai, H. 2001, A&A, 366, 83

Hirashita, H., Buat, V., & Inoue, A.K. 2003, A&A, 410, 83

Hopkins, A. M., et al. 2003, ApJ, 599, 971

Hummer, D.G., & Storey, P.J. 1987, MNRAS, 224, 801

Iglesias-Páramo, J., et al. 2006, ApJS, 164, 38

Inoue, A. K., Hirashita, H., & Kamaya, H. 2001, ApJ, 555, 613

Inoue, A. K. 2001, AJ, 122, 1788

Jansen, R.A., Fabricant, D., Franx, M., & Caldwell, N. 2000, ApJS, 126, 331

Johnson, B.D., et al. 2007a, ApJS, 173, 392

Johnson, B.D., et al. 2007b, ApJS, 173, 377

Johnson, B.D., et al. 2009, in preparation

Jonsson, P., Groves, B., & Cox, T. J. 2009, MNRAS, submitted (arXiv:0906.2156)

Kauffmann, G., et al. 2003, MNRAS, 346, 1055

Kennicutt, R. C. 1983, ApJ, 272, 54

Kennicutt, R. C. 1989, ApJ, 344, 685

Kennicutt, R. C. 1998a, ARA&A, 36, 189

Kennicutt, R. C. 1998b, ApJ, 498, 541

Kennicutt, R. C. 1992, ApJ, 388, 310

Kennicutt, R. C., Lee, J.C., Funes, J.G., Sakai, S., & Akiyama, S. 2008, ApJS, 178, 247

Kennicutt, R. C., & Skillman, E. D. 2001, AJ, 121, 1461

Kennicutt, R. C., Tamblyn, P., & Congdon, C.E. 1994, ApJ, 435, 22

Kennicutt, R. C., et al. 2003, PASP, 115, 98

Kennicutt, R. C., et al. 2007, ApJ, 671, 333

Kewley, L.J., Heisler, C.A., Dopita, M.A., & Lumsden, S. 2001, ApJS, 132, 37

Kewley, L.J., Geller, M.J., Jansen, R.A., & Dopita, M.A. 2002, AJ, 124, 3135

Kewley, L.J., Geller, M.J., & Jansen, R.A. 2004, AJ, 127, 2002

Kong, X., Charlot, S., Brinchmann, J., & Fall, S.M. 2004, MNRAS, 349, 769

Kroupa, P., & Weidner, C. 2003, ApJ, 598, 1076

Lagache, G., Puget, J.-L., & Dole, H. 2005, ARA&A, 43, 727

Lee, H., Skillman, E. D., & Venn, K. A. 2006, ApJ, 642, 813

Leitherer, C., et al. 1999, ApJS, 123, 3

Lonsdale Person, C.J., & Helou, G. 1987, ApJ, 314, 513

Lonsdale, C.J., et al. 2003, PASP, 115, 897

Ly, C., et al., 2007, ApJ, 657, 738

MacArthur, L. 2005, ApJ, 623, 795

Madden, S. 2000, NewAR, 44, 249

Martin, D. C., et al. 2005, ApJ, 619, L1

Mattila, K., Lehtinen, K., & Lemke, D. 1999, A&A, 342, 643

McCall, M. L., Rybski, P. M., & Shields, G. A. 1985, ApJS, 57, 1

Meurer, G.R., Heckman, T.M., & Calzetti, D. 1999, ApJ, 521, 64

Miller, B. W., & Hodge, P. 1996, ApJ, 458, 467

Moshir, M., et al. 1990, IRAS Faint Source Catalogue, version 2.0

Moustakas, J., & Kennicutt, R. C. 2006, ApJS, 164, 81 (MK06)

Moustakas, J., Kennicutt, R.C., Calzetti, D., Dale, D.A., Prescott, M., Smith, J.-D.T., & Tremonti, C.A. 2009, in preparation

Moustakas, J., Kennicutt, R.C., & Tremonti, C.A. 2006, ApJ, 642, 775

Niklas, S., Klein, U., & Wielebinski, R. 1997, A&A, 322, 19

O'Donnell, J.E. 1994, ApJ, 422, 158

Oey, M. S., & Kennicutt, R. C. 1993, ApJ, 411, 1370

Peeters, E., Spoon, H.W.W., & Tielens, A.G.G.M. 2004, ApJ, 613, 986

Peimbert, A., Peimbert, M., & Ruiz, M. T. 2005, ApJ, 634, 1056

Pérez-Gonález, P.G., et al. 2006, ApJ, 648, 987

Popescu, C. C., et al. 2005, ApJ, 619, L75

Prescott, M.P., et al. 2007, ApJ, 668, 182

Relaño, M., Lisenfeld, U., Pérez-González, P.G., Vílchez, J. M., & Battaner, E. 2007, ApJ, 667, L141

Rice, W., Lonsdale, C. J., Soifer, B. T., Neugebauer, G., Kopan, E. L., Lloyd, L. A.; de Jong, T., & Habing, H. J. 1988, ApJS, 68, 91

Rieke, G.H., Alonso-Herrero, A., Weiner, B.J., Perez-Gonzalez, P.G., Blaylock, M., Donley, J.L., & Marcillac, D. 2009, ApJ, 692, 556

Roussel, H., Sauvage, M., Vigroux, L., & Bosma, A. 2001, A&A, 372, 427

Salpeter, E.E. 1955, ApJ, 121, 161

Sanders, D.B., Mazzarella, J.M., Kim, D.-C., Surace, J.A., & Soifer, B.T. 2003, AJ, 126, 1607

Sauvage, M., & Thuan, T.X. 1992, ApJ, 396, 69

Smith, J. D. T., et al. 2007, ApJ, 656, 770

Soifer, B. T., Boehmer, L., Neugebauer, G., & Sanders, D. B. 1989, AJ, 98, 766

Soifer, B.T., Neugebauer, G., & Houck, J.R. 1987, ARA&A, 25, 187

Stasińska, G., Comte, G., & Vigroux, L. 1986, A&A, 154, 352

Stauffer, J. R., & Bothun, G. D. 1984, AJ, 89, 1702

Terlevich, R., Melnick, J., Masegosa, J., Moles, M., & Copetti, M. V. F. 1991, A&AS, 91, 285

Tuffs, R.J., Popescu, C.C., Völk, H.J., Kylafis, N.D., & Dopita, M.A., 2004, A&A, 419, 821

van Zee, L., Haynes, M. P., & Salzer, J. J. 1997, AJ, 114, 2479

van Zee, L., Salzer, J. J., Haynes, M. P., O'Donoghue, A. A., & Balonek, T. J. 1998, AJ, 116, 2805

Wang, B., & Heckman, T. 1996, ApJ, 457, 645

Webster, B. L., & Smith, M. G. 1983, MNRAS, 204, 743

Wild, V., Kauffmann, G., Heckman, T., Charlot, S., Lemson, G., Brinchmann, J., Reichard, T., & Pasquali, A. 2007, MNRAS, 381, 543

Witt, A.N., Thronson, H.A., & Capuano, J.M. 1992, ApJ, 393, 611

Witt, A.N., & Gordon, K.D. 2000, ApJ, 528, 799

Wu, H., Cao, C., Hao, C.-N., Liu, F.-S., Wang, J.-L., Xia, X.-Y., Deng, Z.-G., & Young, C.K.-S. 2005, ApJ, 632, L79

Wu, Y., Charmandaris, V., Hao, L., Brandl, B. R., Bernard-Salas, J., Spoon, H. W. W., & Houck, J. R. 2006, ApJ, 639, 157

Young, J.S., Allen, L., Kenney, J.D.P., Lesser, A., & Rownd, B. 1996, AJ, 112, 1903

Yun, M. S., Reddy, N. A., & Condon, J. J. 2001, ApJ, 554, 803

Zaritsky, D., Harris, J., Thompson, I.B., Grebel, E.K., & Massey, P. 2002, AJ, 123, 855

Zaritsky, D., Kennicutt, R. C., & Huchra, J. P. 1994, ApJ, 420, 87

Zhu, Y.-N., Wu, H., Cao, C., & Li, H.-N. 2008, ApJ, 686, 155

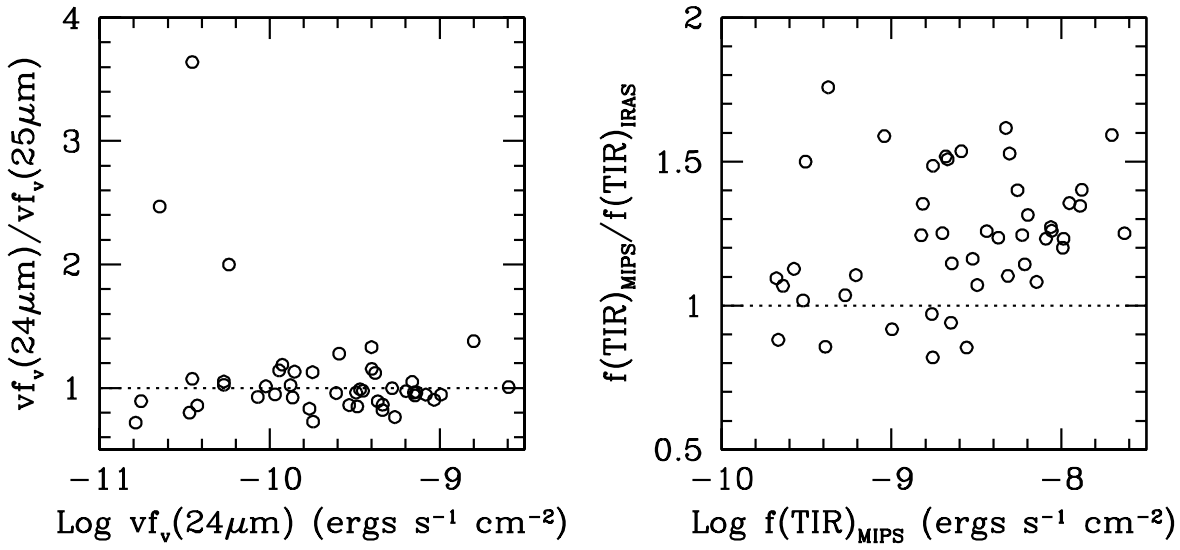

Fig. 1.— *Left:* Ratio of MIPS 24 μm flux to *IRAS* 25 μm flux for SINGS galaxies, plotted as a function of MIPS (apparent) flux. *Right:* Ratio of MIPS total infrared (TIR) flux to *IRAS* TIR flux for galaxies in the same sample.

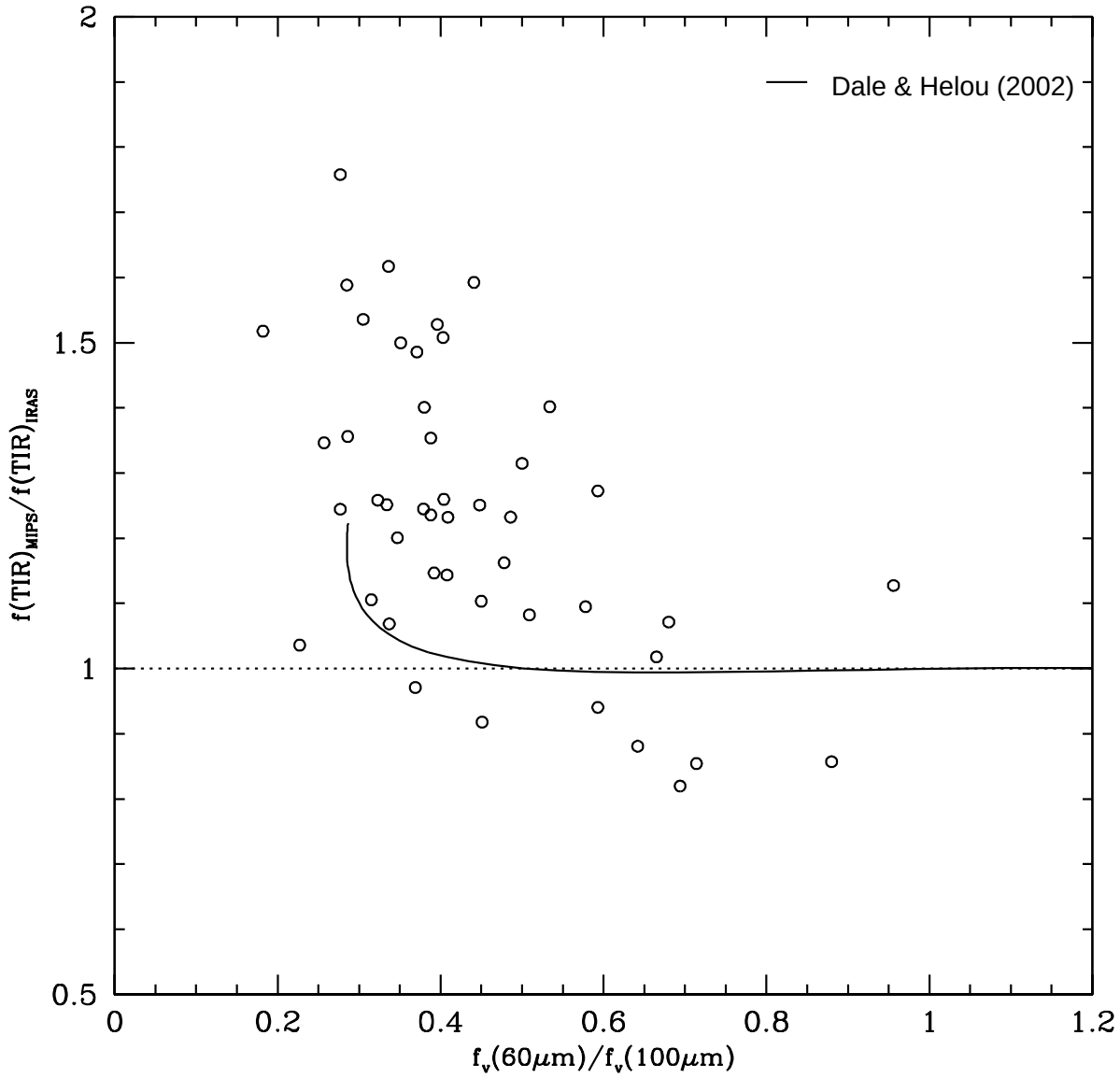

Fig. 2.— Ratio of MIPS total infrared (TIR) flux to *IRAS* TIR flux for SINGS galaxies, calculated using the prescriptions of Dale & Helou (2002), plotted as a function of *IRAS* 60 μm to 100 μm flux ratio. Note that the galaxies with the largest discrepancies possess relatively cold dust temperatures (low $f_\nu(60\,\mu\mathrm{m})/f_\nu(100\,\mu\mathrm{m})$ ratios). The solid line shows the expected relation based on SED models in Dale & Helou. Many of the SINGS galaxies with the coldest $f_\nu(60\,\mu\mathrm{m})/f_\nu(100\,\mu\mathrm{m})$ colors appear to show even larger discrepancies.

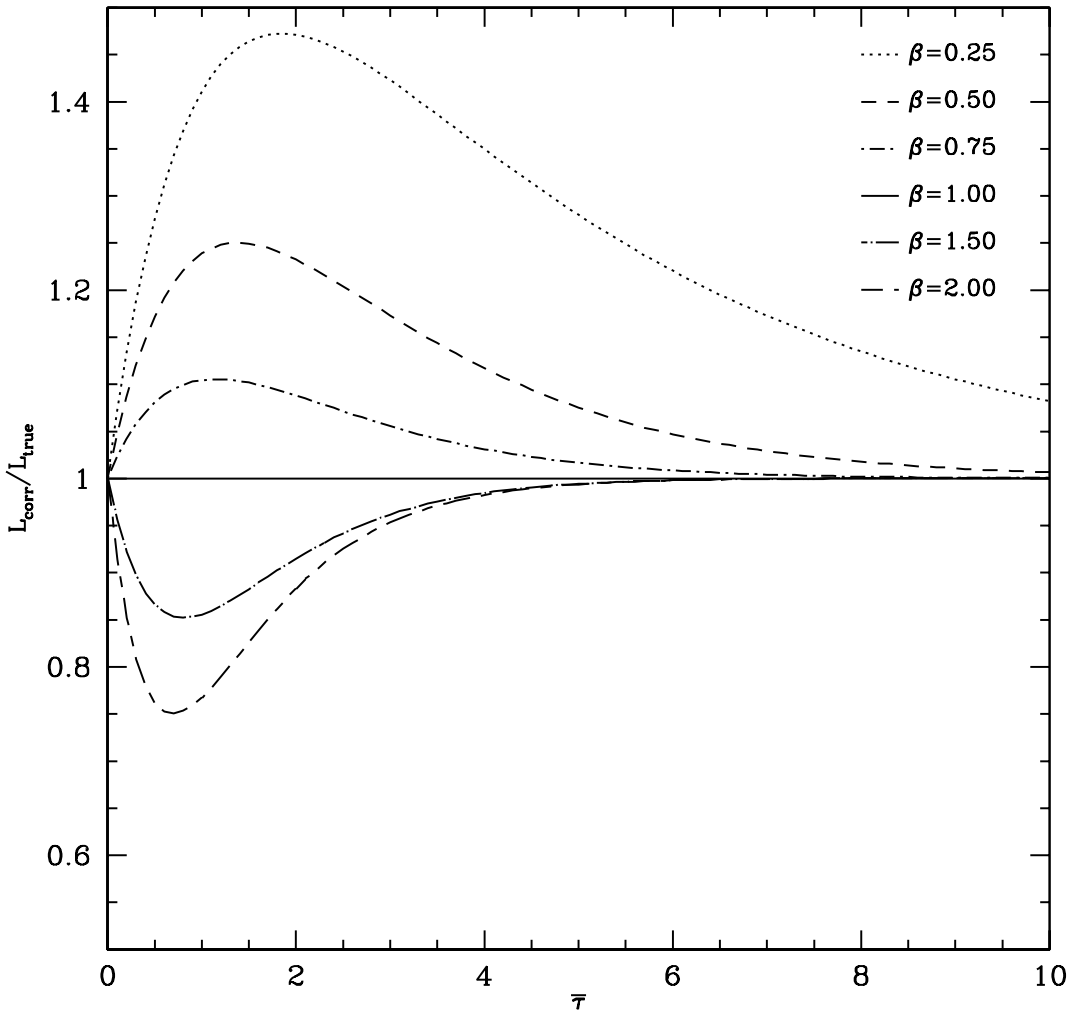

Fig. 3.— These curves show the approximate magnitude of the systematic error in attenuation-corrected SFRs introduced by applying a linear combination of optical emission-line and IR continuum fluxes of galaxies to estimate the mean attenuation. The curves are parameterized by the ratio of the attenuation in the emission-line to that of the average dust heating continuum (β). The linear combination is an exact relation when the two opacities match ($\beta = 1$).

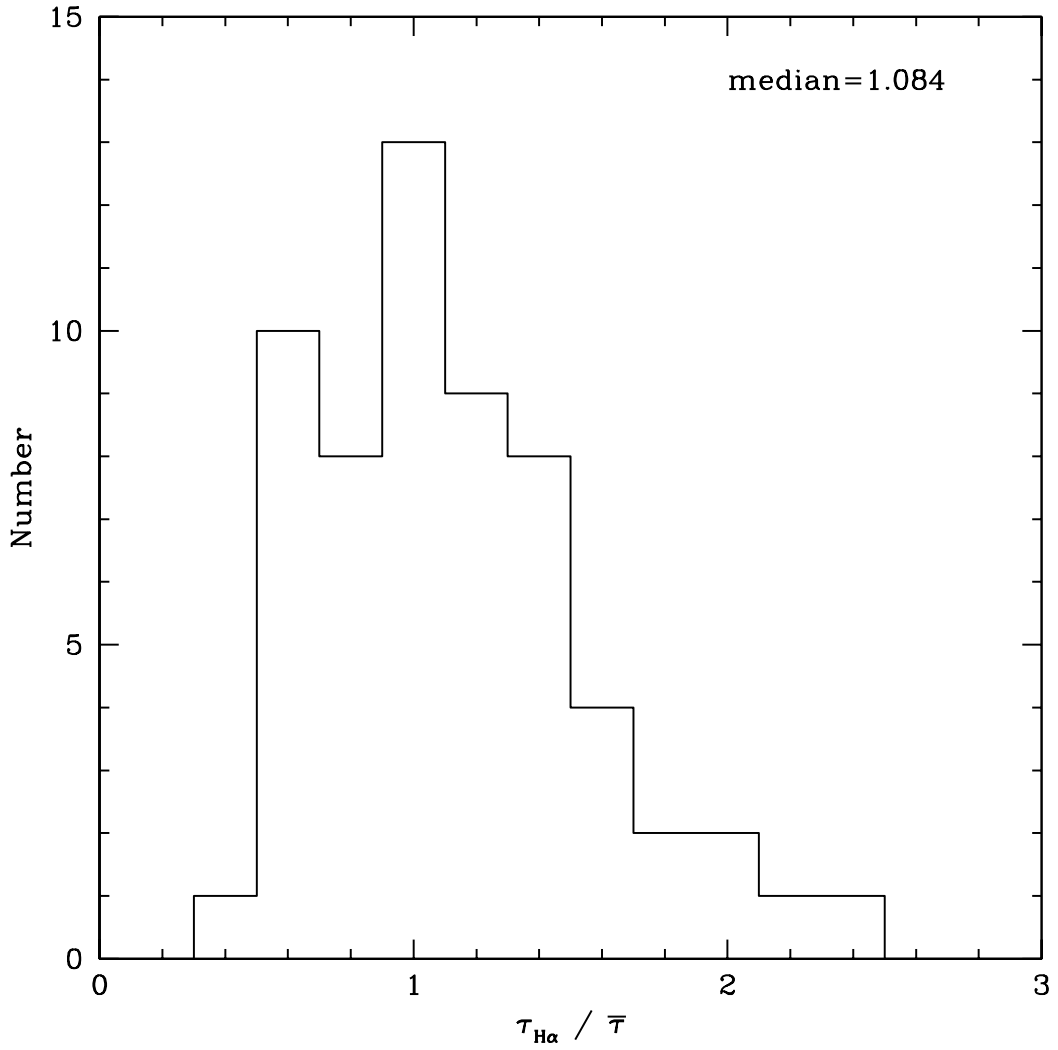

Fig. 4.— Histogram of ratios of dust attenuation in the Hα emission line, as estimated from the Balmer decrement as described in the text, to the mean continuum dust opacity, estimated from the bolometric fraction of IR emission in the SED of each MK06 galaxy. The median value shows that the galaxies lie close to the $\beta = 1$ case.

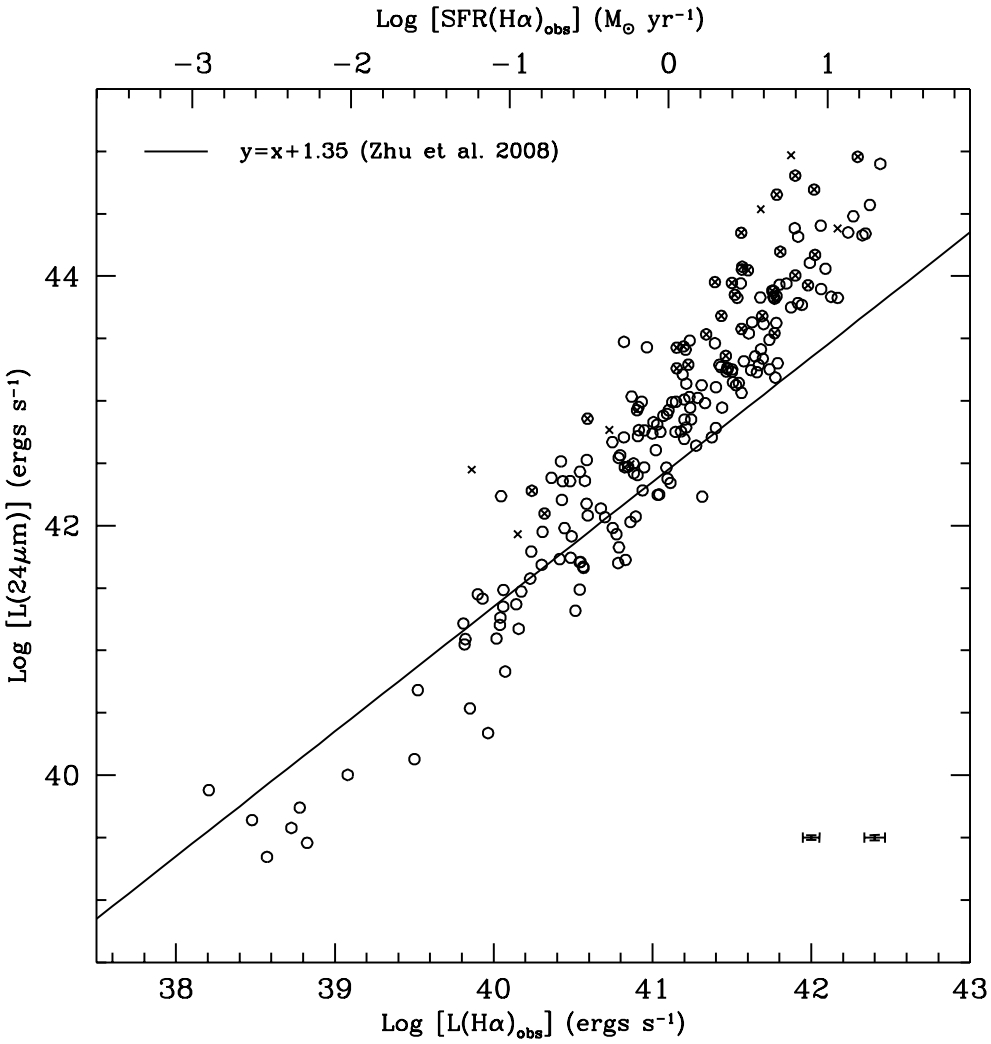

Fig. 5.— Relation between observed 24 μm infrared luminosity and observed Hα luminosity (uncorrected for attenuation) for galaxies in the SINGS and MK06 samples. Symbol shapes are coded by dominant emission-line spectral type: circles for HII region like spectra, crosses for spectra with strong AGN signatures, and crossed circles for galaxies with composite spectra. The solid line shows a relationship with linear slope, to illustrate the strong nonlinearity in the observed relation. The axis label at the top of the diagram shows the approximate range of SFRs (absent a correction for dust attenuation at Hα) for reference.

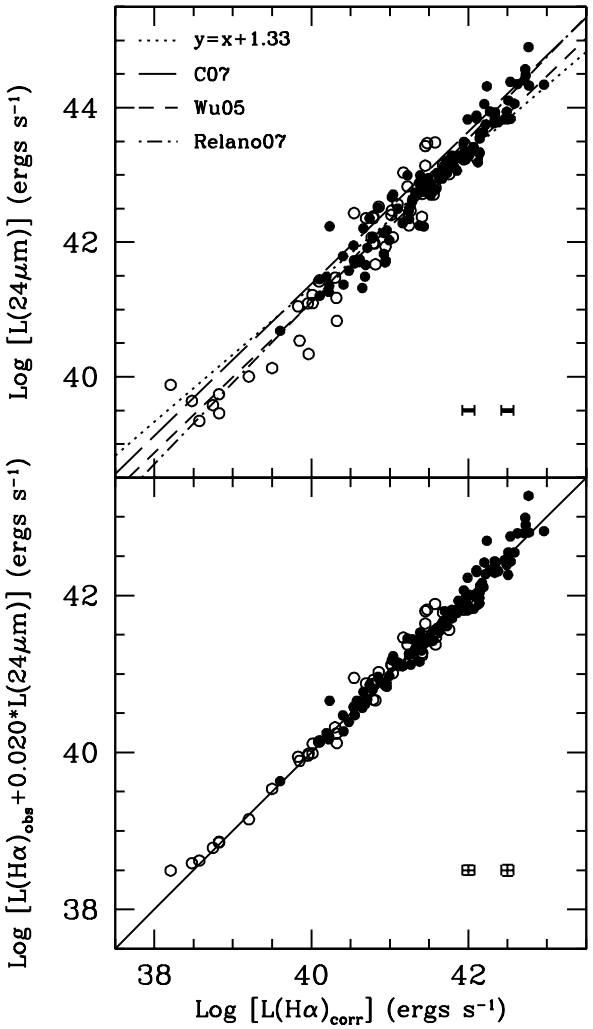

Fig. 6.— *Top:* Relation between observed 24 μm IR luminosity and attenuation-corrected Hα luminosity for star formation dominated SINGS galaxies (open circles) and MK06 galaxies (solid circles). The attenuation corrections were derived from the absorption-corrected Hα/Hβ ratios in the optical spectra. The dotted line shows a linear relation for comparison, while the solid line shows the best fitting nonlinear relation for HII regions in C07. The other two lines show published fits to other galaxy samples. The error bars in the lower right show typical 1-σ uncertainties for individual measurements of SINGS sample (left) and MK06 sample (right). *Bottom:* Linear combination of (uncorrected) Hα and 24 μm luminosities compared to the same Balmer-attenuation-corrected Hα luminosities, with the scaling coefficient a (eq. [1]) derived from a median fit to the linear relation. Note the tightness of the relation over nearly the entire luminosity range.

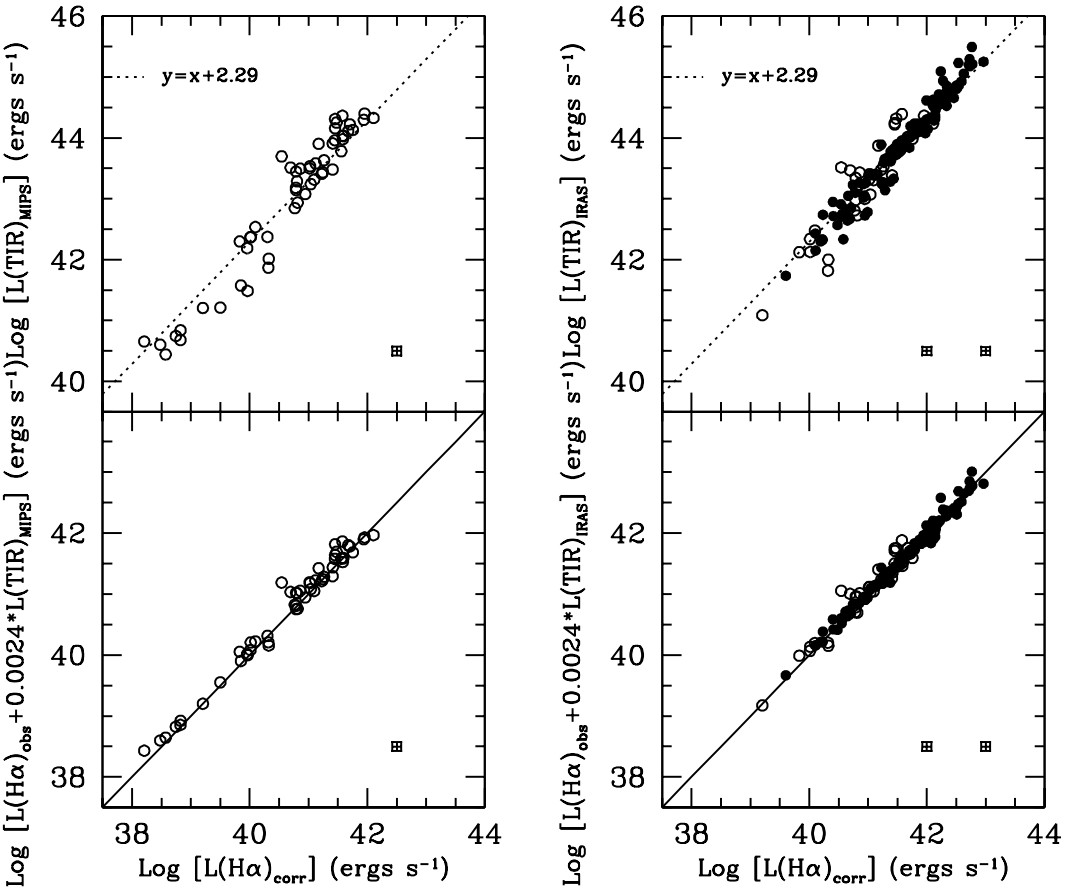

Fig. 7.— The same comparison as in Figure 6, but comparing total infrared (TIR) and Hα luminosities, in place of 24 μm vs Hα luminosities. The left-hand pair of plots are for *Spitzer* MIPS TIR measurements of the SINGS sample, while the right-hand pair of plots show corresponding *IRAS* TIR measurements of the SINGS and MK06 samples. The SINGS samples are slightly different in the two cases because not all SINGS galaxies were detected by IRAS. As in Figure 6 the top panels compare the observed TIR and Balmer-corrected Hα luminosities, while the bottom panels compare linear combinations of (uncorrected) Hα and IR luminosities with the Balmer-corrected Hα luminosities. Open circles denote SINGS galaxies and solid circles MK06 galaxies.

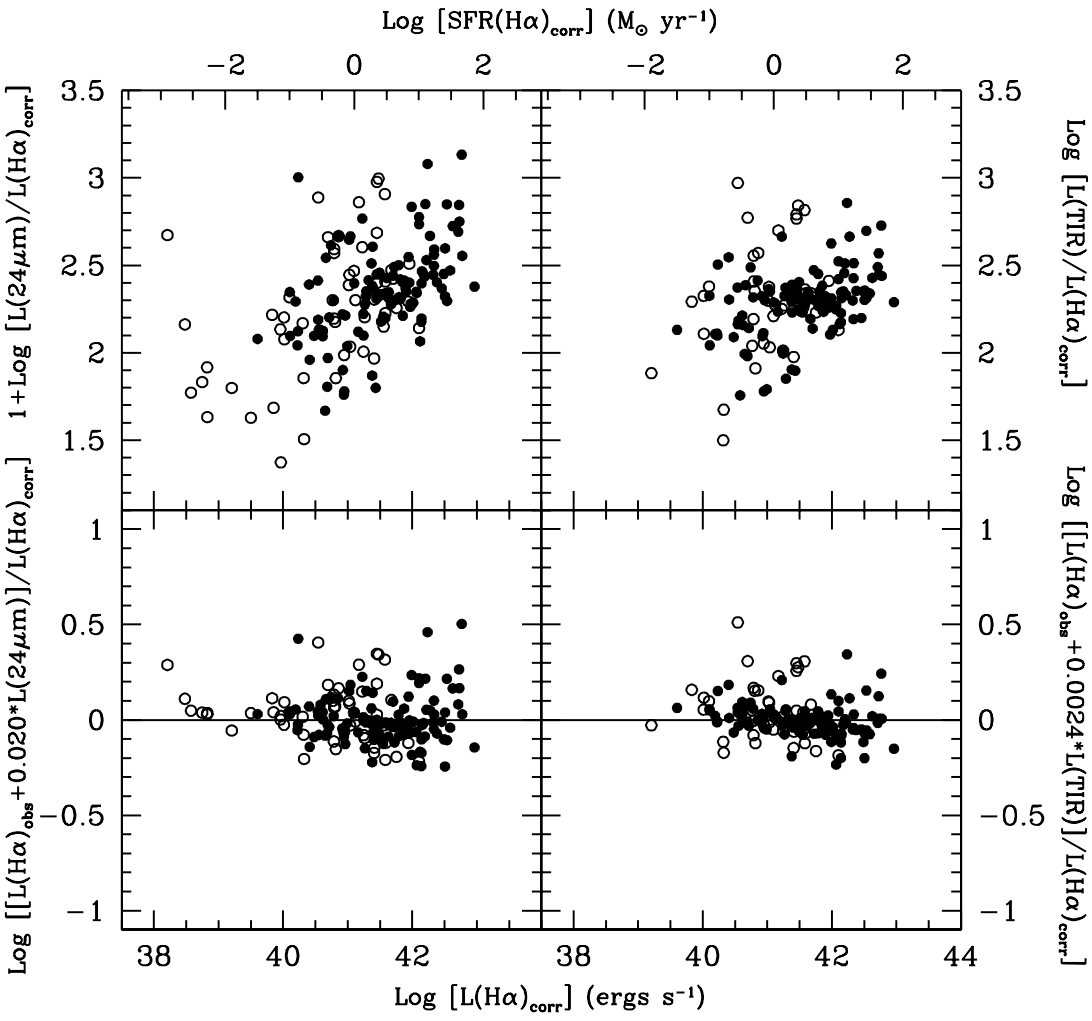

Fig. 8.— Residuals from the comparisons shown in Figure 6 (left panels, 24 μm and Hα) and Figure 7 (right panels, *IRAS* TIR and Hα). Open circles denote SINGS galaxies and solid circles denote MK06 galaxies.

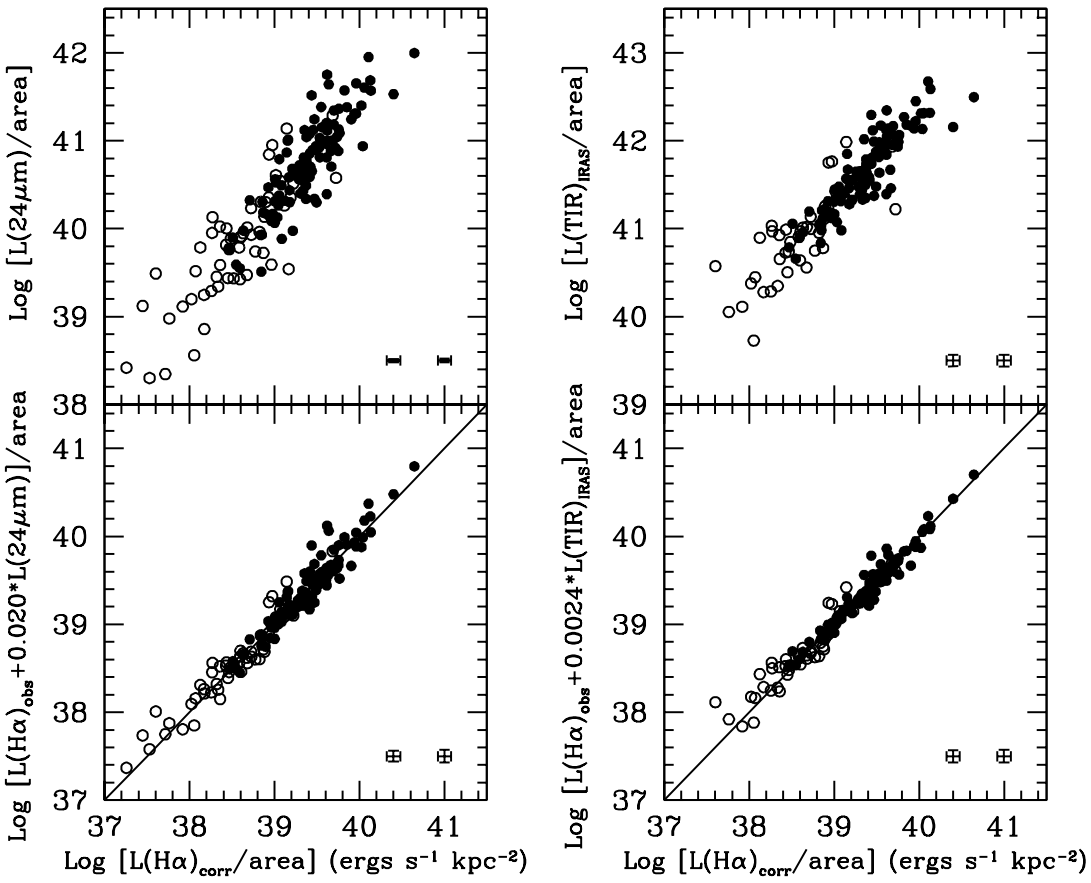

Fig. 9.— Similar to Figures 6 and 7, but comparing galaxy surface brightnesses rather than luminosities. The top panels show 24 μm (left) and TIR (right) surface brightnesses as a function of Balmer-corrected Hα surface brightness, for SINGS galaxies (open circles) and MK06 galaxies (solid circles). The bottom panels compare attenuation-corrected Hα surface brightnesses as derived from linear combinations of Hα + 24 μm fluxes (left) and Hα + TIR fluxes (right) with those derived from the absorption- corrected Balmer decrements.

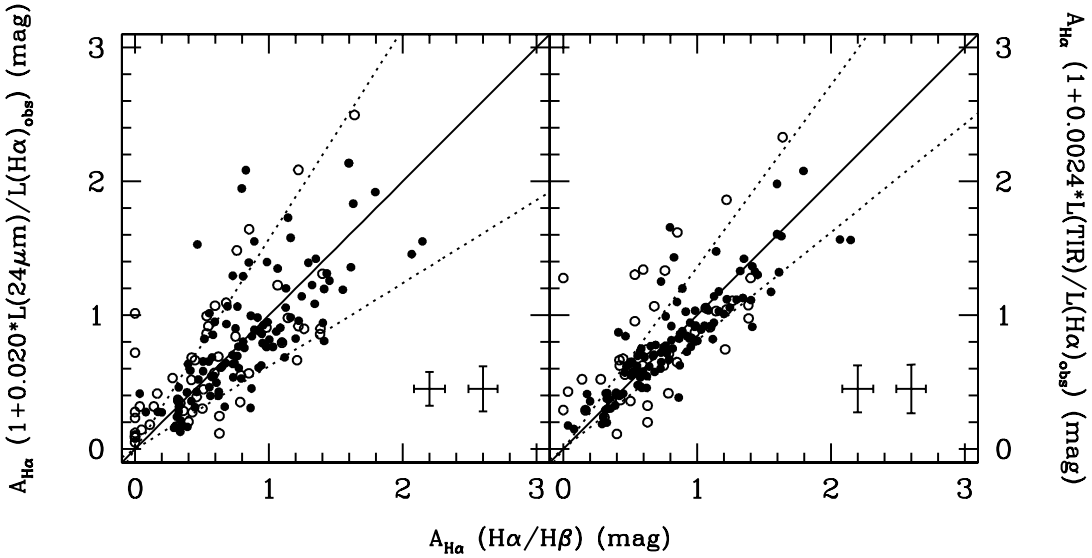

Fig. 10.— Comparison of Hα dust attenuations estimated from eq. (2) using 24 μm and uncorrected Hα fluxes (left panel) and *IRAS* TIR and uncorrected Hα fluxes (right panel), in each case compared to attenuations estimated from the absorption-corrected Hα/Hβ ratio. Open circles denote SINGS galaxies and solid circles denote MK06 galaxies. The dotted lines contain 68% of the galaxies, corresponding approximately to 1-σ dispersions unit-slope relation.

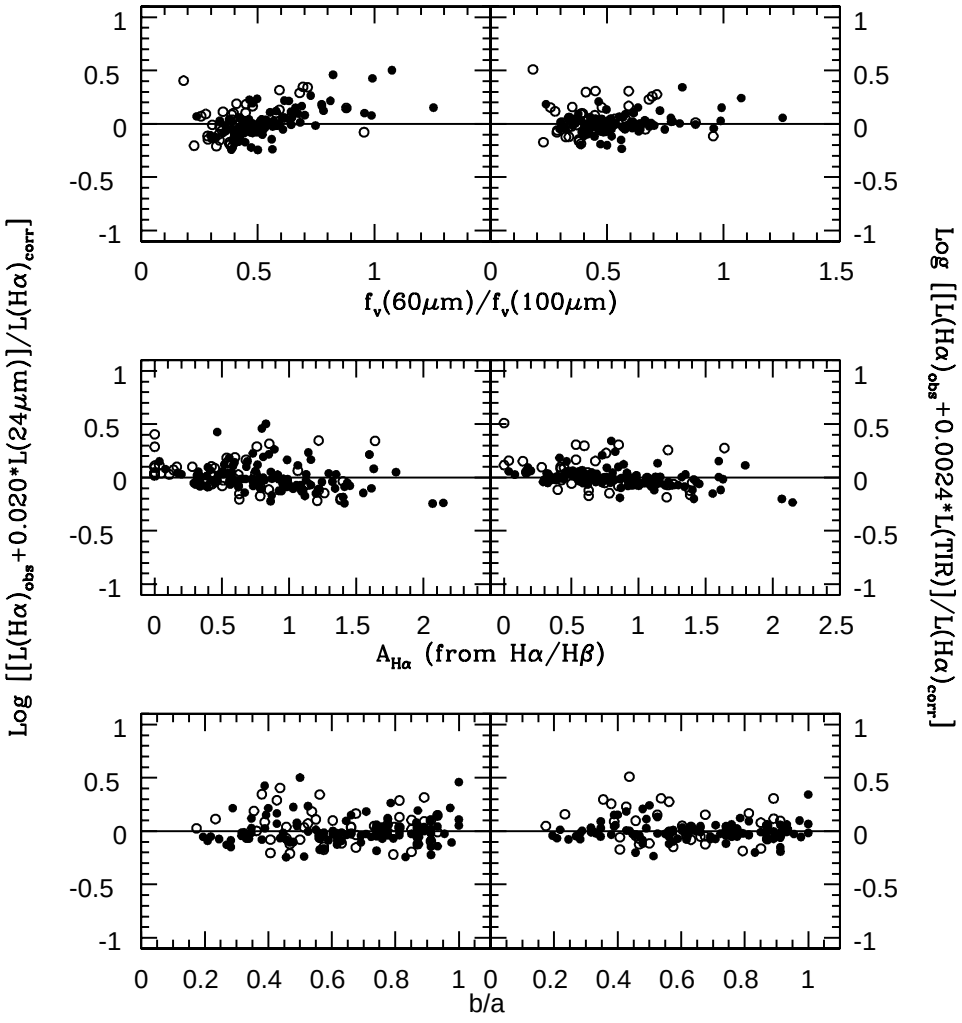

Fig. 11.— Ratios of attenuation-corrected Hα luminosities derived from the combination of observed Hα and IR fluxes, to those derived from the Balmer decrements, plotted as functions of infrared color (top panels), Balmer attenuation (middle panels), and galaxy axial ratio (bottom panels). The left panels show residuals using 24 μm + Hα, while the right panels show the corresponding residuals using TIR + Hα combination. Open circles denote SINGS galaxies and solid circles denote MK06 galaxies.

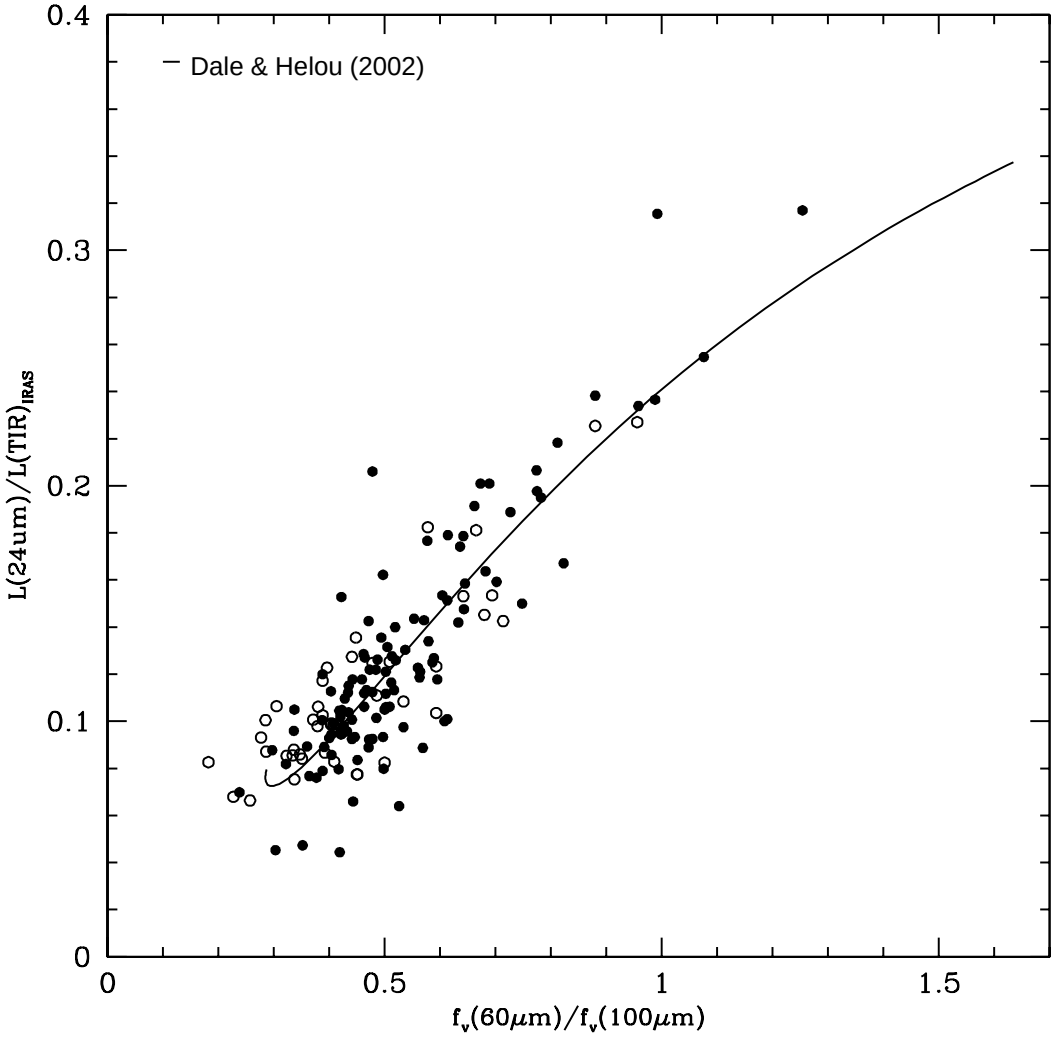

Fig. 12.— Ratios of 24 μm dust luminosity (νL_ν) to total infrared (TIR) luminosities of galaxies in our sample, plotted as a function of 60 μm/100 μm color. Open circles denote SINGS galaxies and solid circles denote MK06 galaxies. The solid line shows the SED template sequence from Dale & Helou (2002).

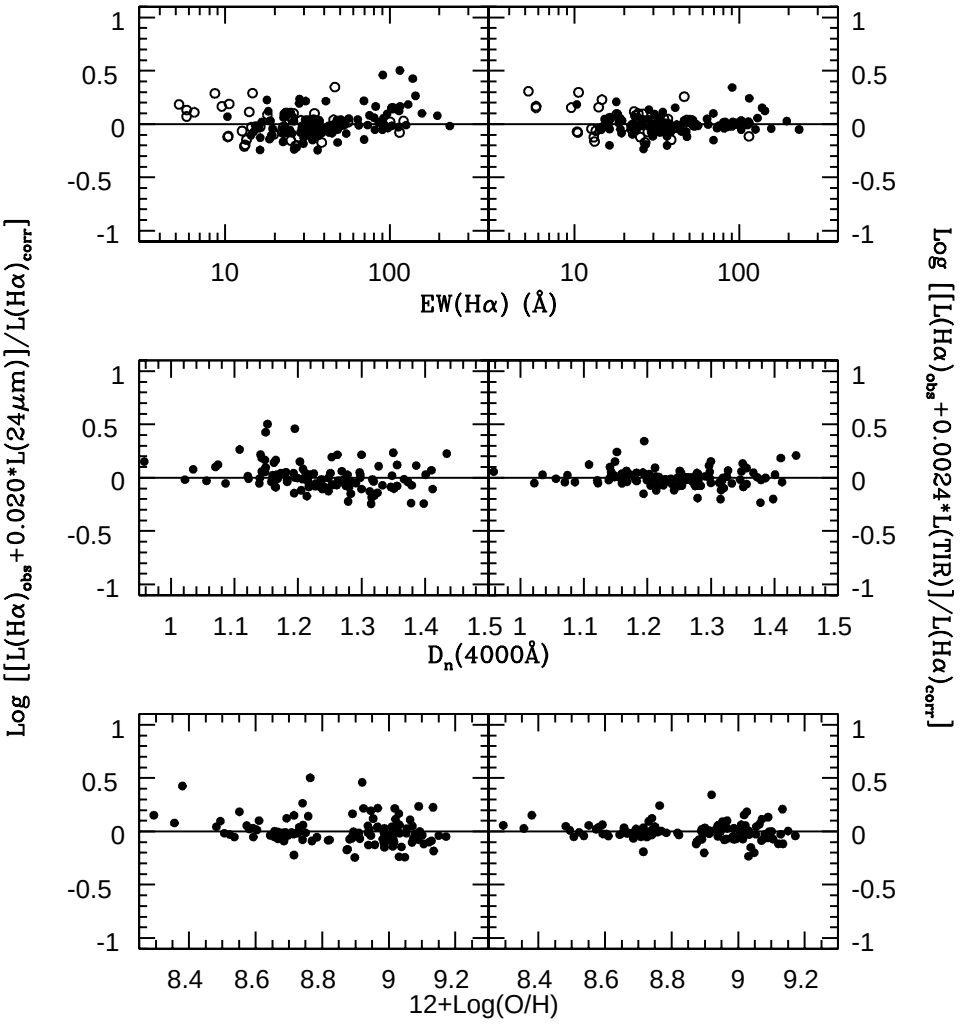

Fig. 13.— Similar to Figure 11, but with residuals plotted as functions of integrated Hα emission-line equivalent width (top panels), 4000 Å discontinuity (middle panels), and average gas-phase oxygen abundance (bottom panels). See Figure 11 for explanation of methods and symbols.

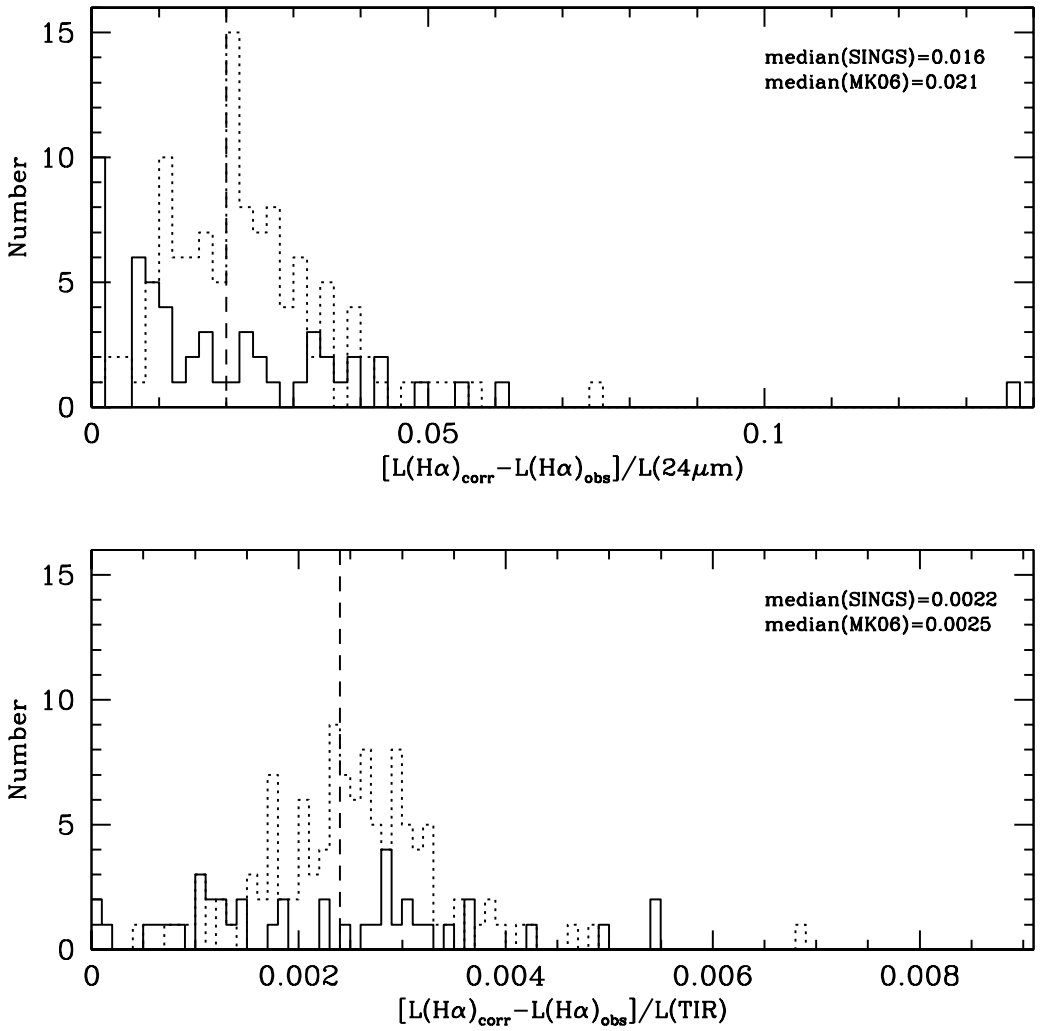

Fig. 14.— Histograms of the scaling constant a in eqs. (1–2), which forces the attenuation derived from the ratio of 24 um/Hα fluxes (top panel) and ratio of TIR/Hα fluxes (bottom panel) to agree with that derived from the Hα/Hβ ratio in the integrated spectrum. Solid lines show the distribution of a values for the SINGS sample, while dotted lines show the corresponding distributions for the MK06 galaxies. The adopted values of a for the combined sample (see Table 4) are shown by vertical dashed lines.

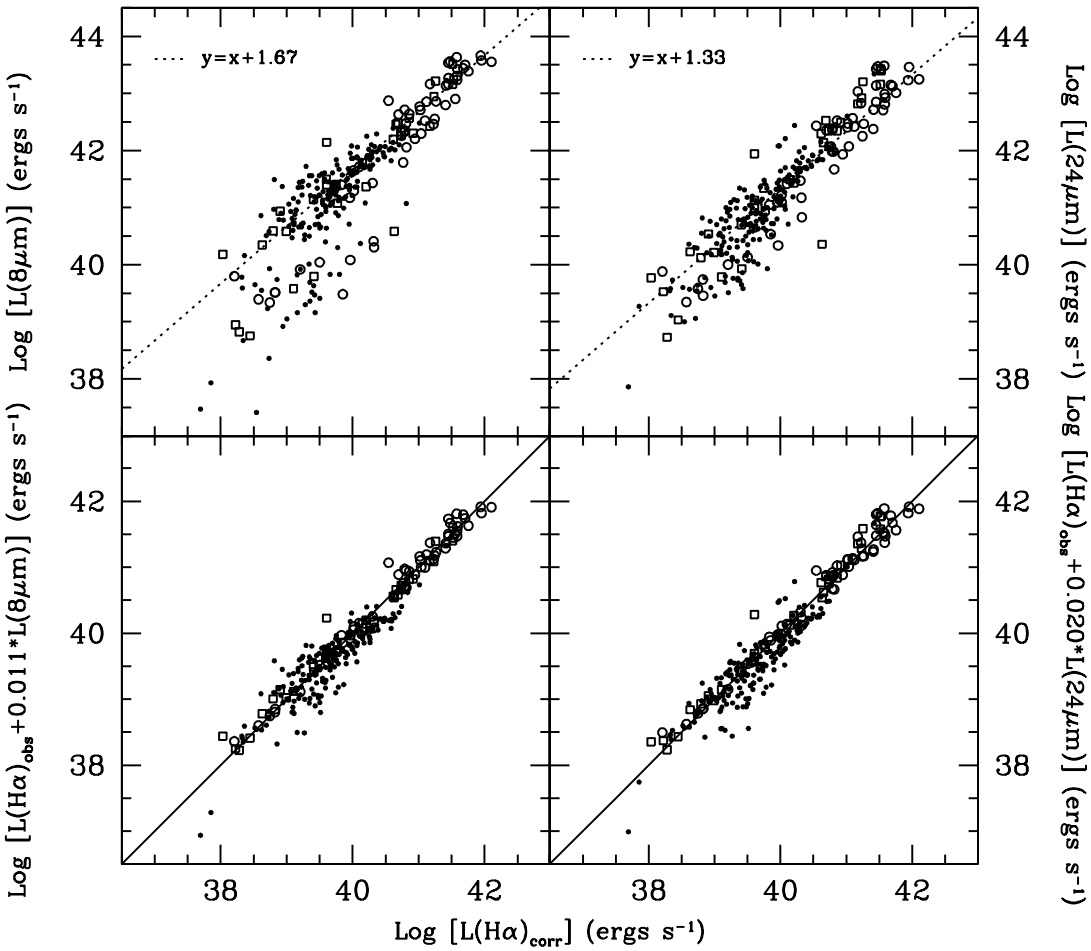

Fig. 15.— *Top Panels:* Observed 8 μm PAH luminosities *(left)* and 24 μm luminosities *(right)* of SINGS galaxies and subregions, plotted as a function of Balmer-corrected Hα luminosities, as in previous figures. Open circles denote integrated measurements of SINGS galaxies, open squares denote measurements of the central $20'' \times 20''$ regions, while small solid points denote individual HII regions from C07. *Bottom Panels:* Best fitting linear combinations of uncorrected Hα and 8 μm *(left)* or 24 μm *(right)* luminosities, as a function of Balmer-corrected Hα luminosities.

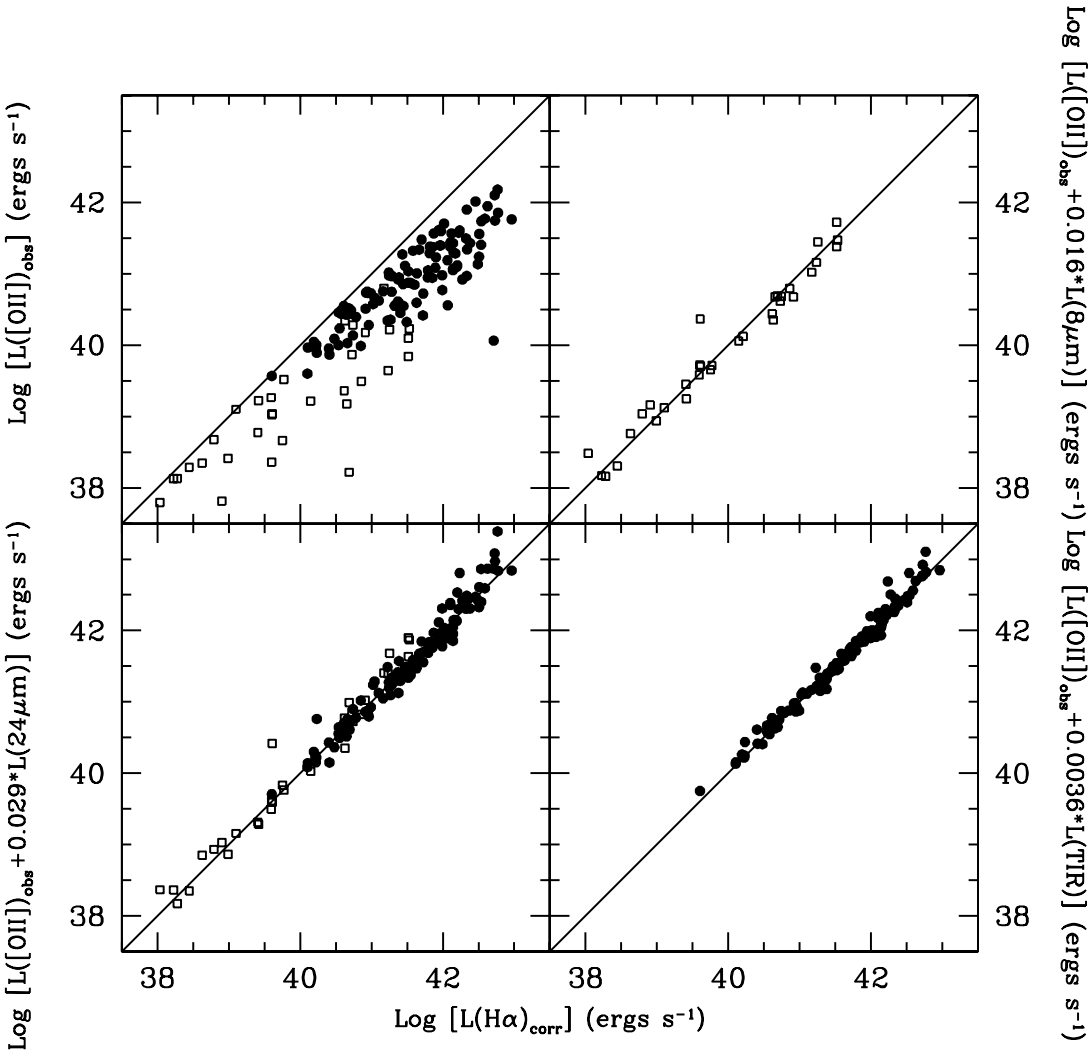

Fig. 16.— *Top Left:* Observed [O II]λ3727 emission-line luminosities of SINGS central 20″ × 20″ regions (open squares) and MK06 (solid circles) galaxies, plotted as a function of Balmer-corrected Hα luminosities, as in previous figures. *Other Panels:* Best fitting linear combinations of observed [O II] luminosities and IR band luminosities, as functions of Balmer-corrected Hα luminosities.

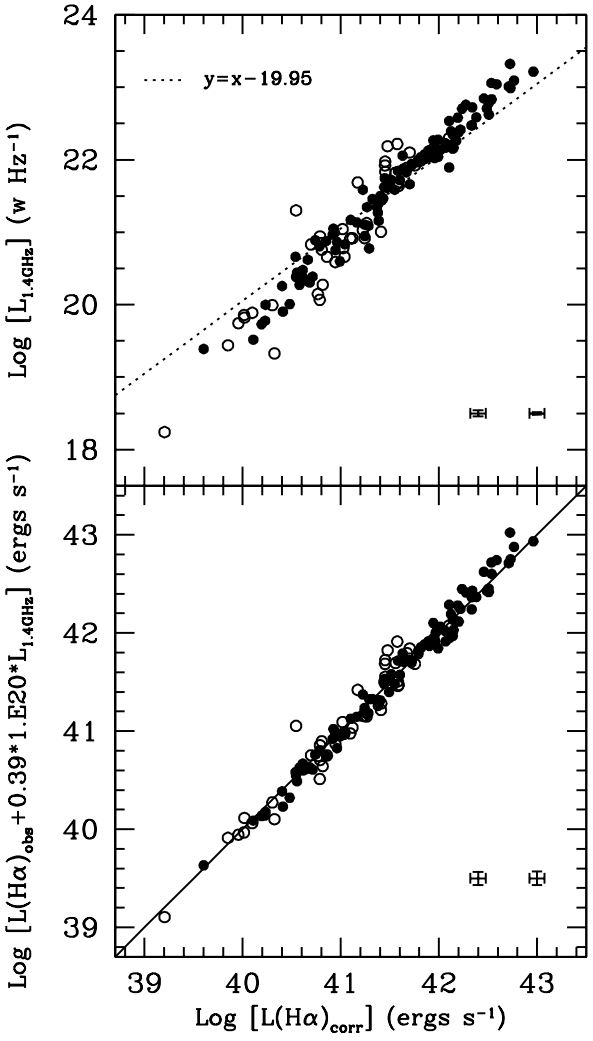

Fig. 17.— *Top:* Integrated 1.4 GHz radio continuum luminosities of SINGS galaxies (open circles) and MK06 galaxies (solid circles) plotted as a function of Balmer-corrected Hα luminosities. The dotted line shows a linear correlation for reference. *Bottom:* Best fitting linear combinations of uncorrected Hα and radio continuum luminosities, as a function of Balmer-corrected Hα luminosities.

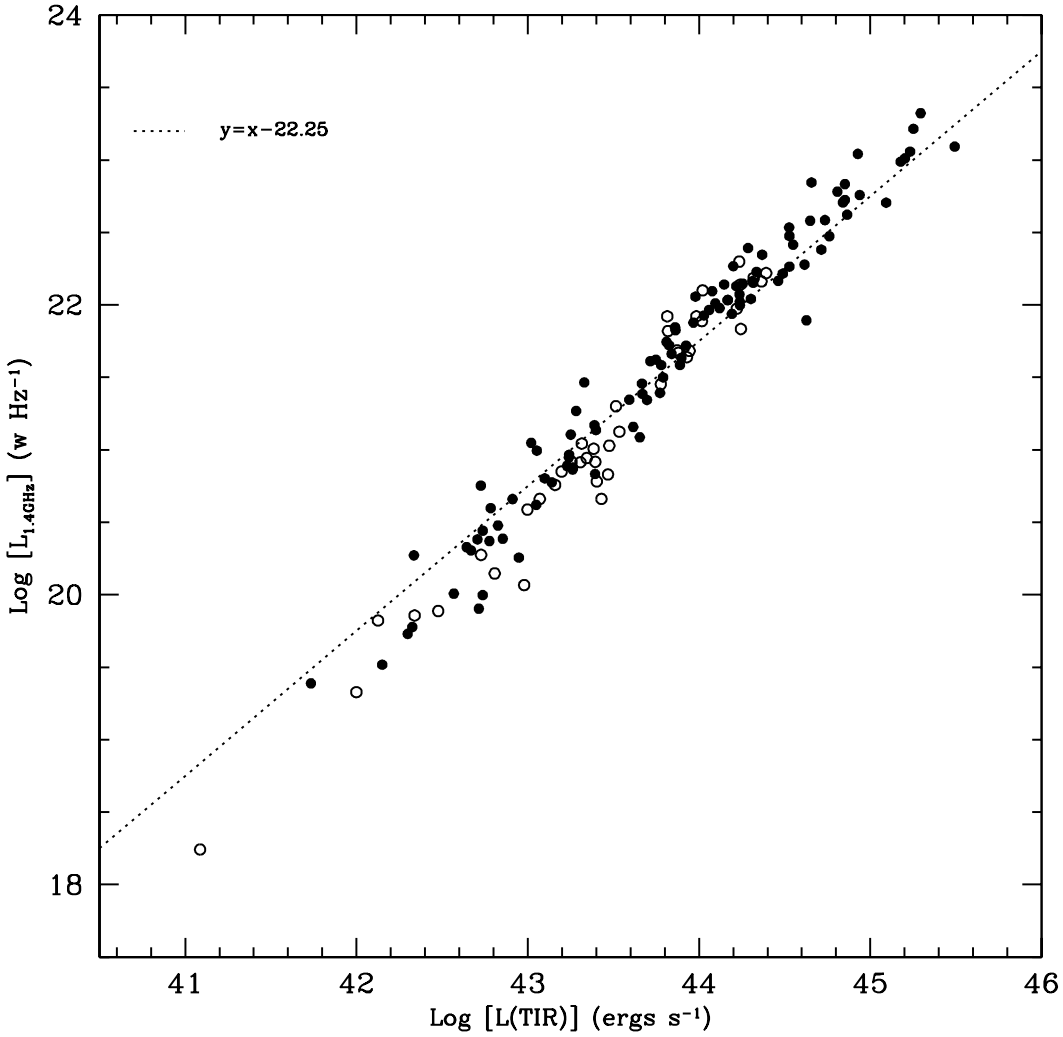

Fig. 18.— Relationship between 1.4 GHz radio continuum luminosity and total infrared (TIR) luminosity for SINGS galaxies (open circles) and MK06 galaxies (solid circles). The dotted line shows a linear correlation for reference.

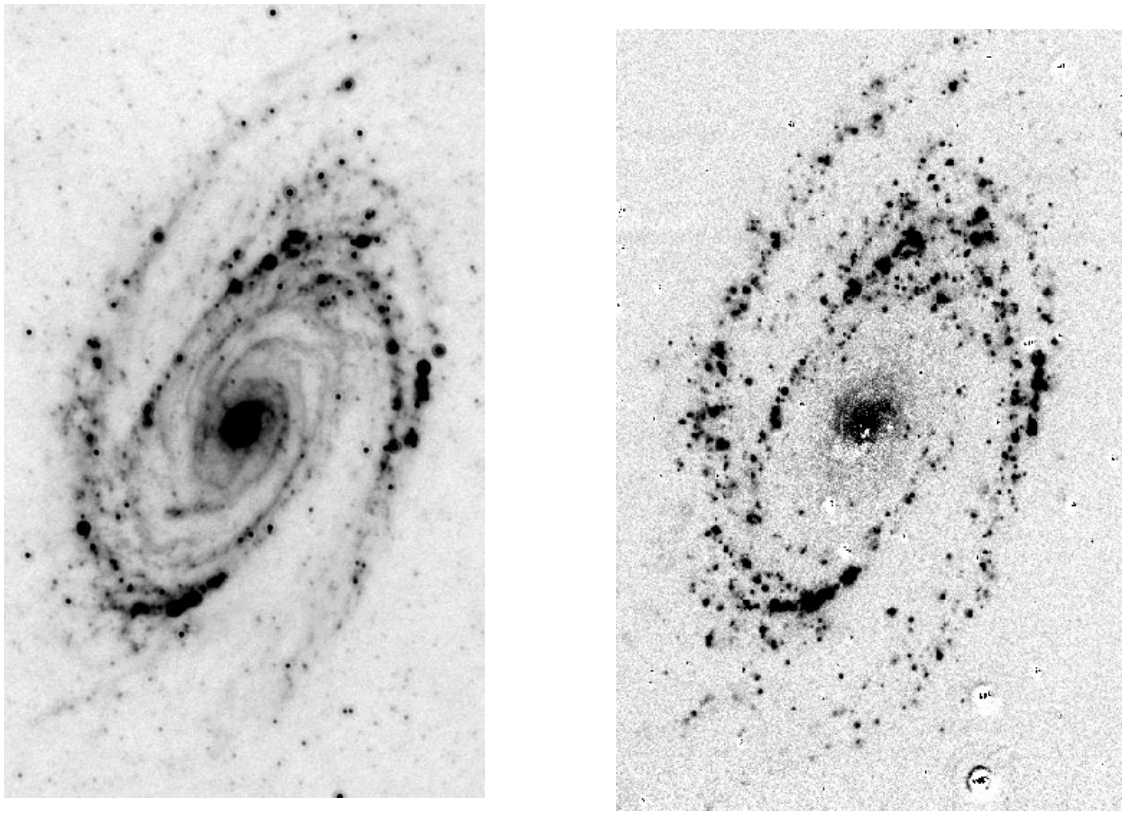

Fig. 19.— SINGS galaxy M81 observed in the mid-infrared at 24 μm *(left)*, and in Hα *(right)*. Note the strong spatial correlation of bright infrared sources with optical HII regions, and the extensive diffuse 24 μm emission in regions devoid of Hα emission.

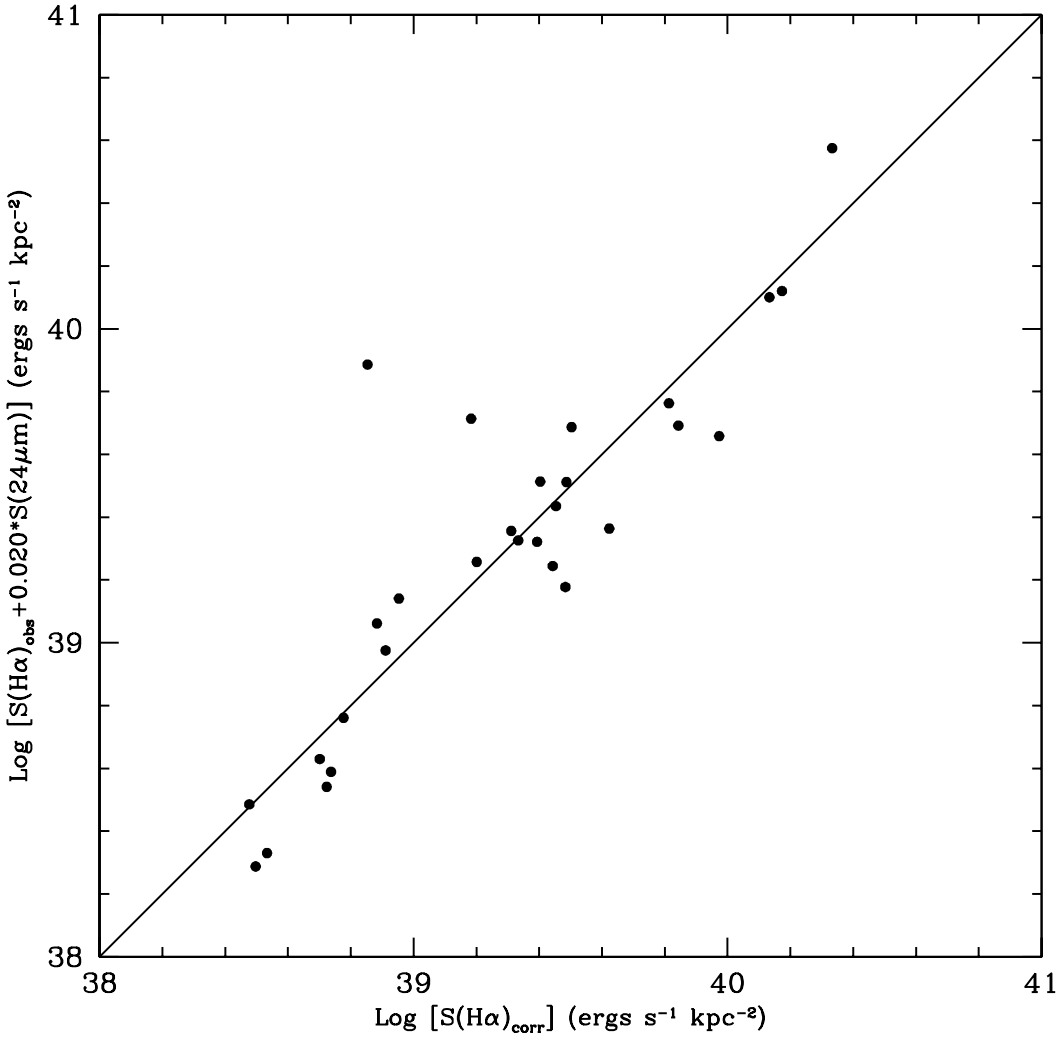

Fig. 20.— Extinction-corrected Hα surface brightnesses for the central $50'' \times 50''$ regions of 29 SINGS galaxies ($\sim 144'' \times 144''$ for NGC 5194), as derived from the observed Hα and 24 μm fluxes, plotted as a function of the attenuation-corrected Hα surface brightnesses as derived from the Pa α/Hα ratio.

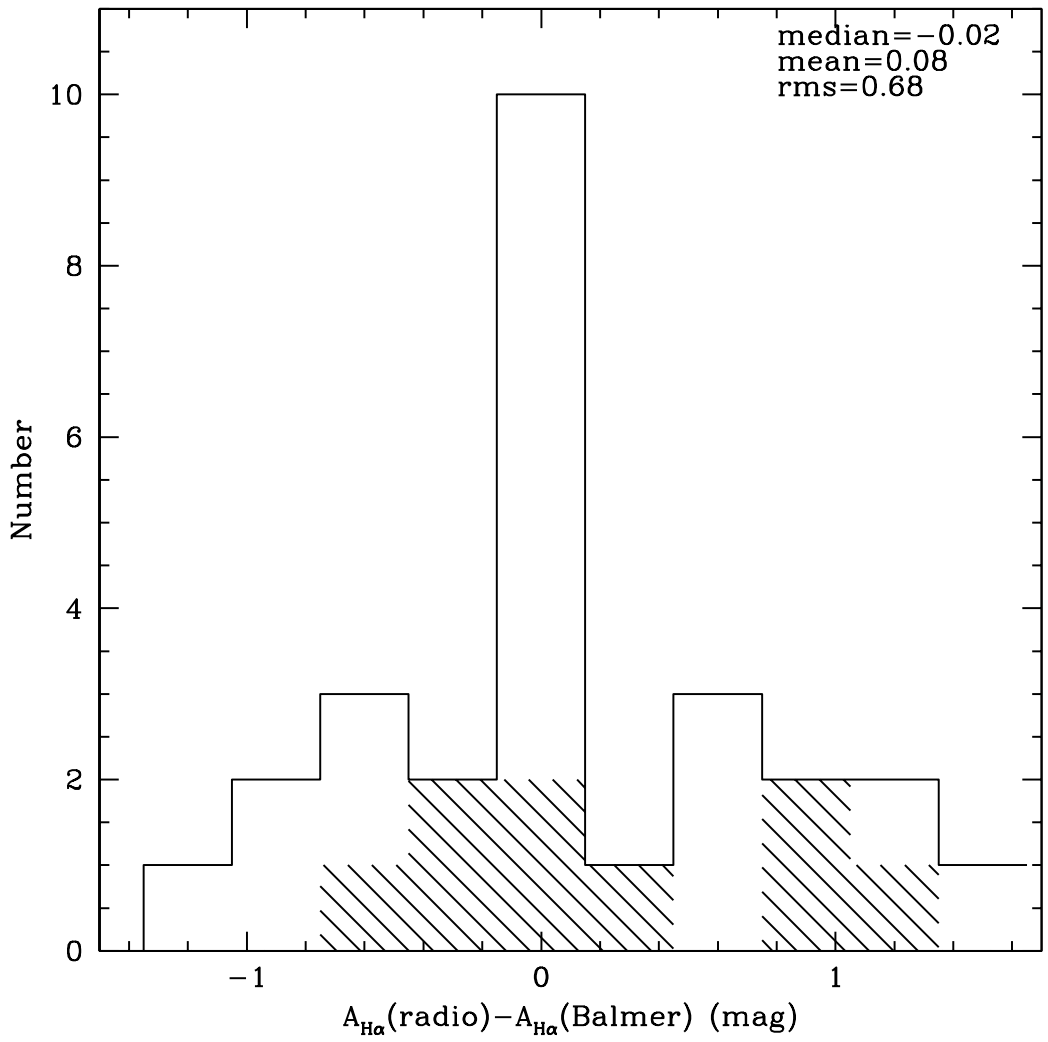

Fig. 21.— Histogram of the differences between the Hα attenuations estimated from the thermal radio to Hα ratios and those from the Hα/Hβ ratios. The hatched histogram denotes the distribution of the nine objects whose thermal fractions are upper limits.

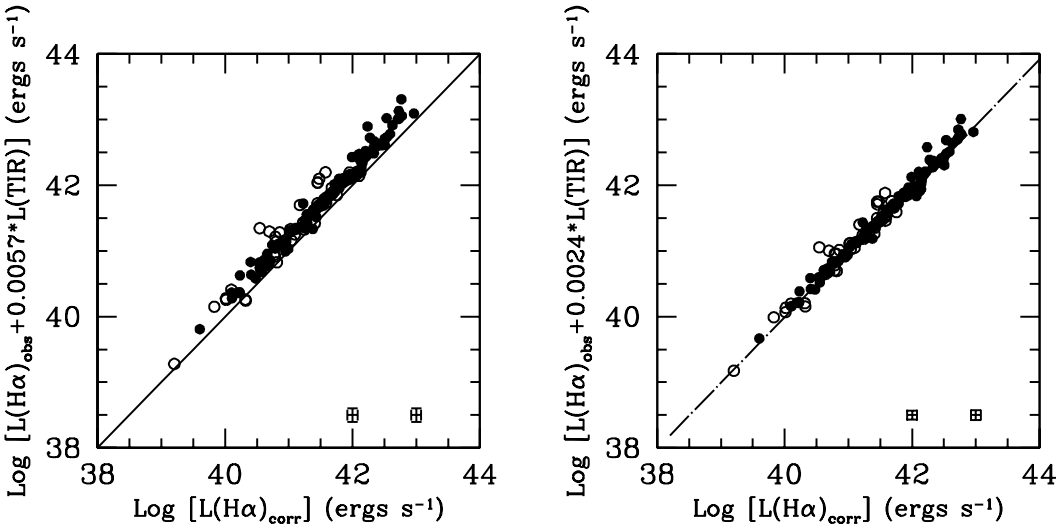

Fig. 22.— *Left:* Comparison of attenuation-corrected Hα luminosities from a combination of Hα and TIR luminosities using coefficients from Kennicutt (1998a) with Balmer-corrected luminosities. The line superimposed shows the expected relation if two sets of luminosities were equal. *Right:* Same comparison but using the empirically measured value for the coefficient a in eq. (1). In this case the line is from a set of dust attenuation and IR emission models from Calzetti et al. (2007), with dust heated by a galaxy with a constant SFR over the past 10 Gyr. In both panels open circles represent SINGS galaxies and solid circles denote MK06 galaxies.

Table 1. Integrated Measurements of SINGS Galaxies

Name	Distance (Mpc)	log(Hα+[NII]) (erg s^{-1} cm^{-2})	Hα/Hβ	[NII]/Hα	S$_\nu$(25 μm) (Jy)	S$_\nu$(60 μm) (Jy)	S$_\nu$(100 μm) (Jy)	references (Hα/Hβ)	references ([NII]/Hα)	references (IRAS)
(1)	(2)	(3)	(4)	(5)	(6)	(7)	(8)	(9)	(10)	(11)
NGC0024	7.3	-11.87±0.04	2.902±0.219	0.373±0.034	0.16±0.046	1.26±0.139	3.59±0.395	3	3	103
NGC0337	22.4	-11.43±0.03	3.465±0.042	0.230±0.004	0.76±0.050	9.07±0.043	20.11±0.387	1	1	101
NGC0628	7.3	-10.84±0.04	3.215±0.225	0.345±0.046	2.87±0.060	21.54±0.045	54.45±0.229	3;5;7;8	5;6;7;8	101
NGC0855	9.73	-12.23±0.04	3.292±0.121	0.185±0.011	···	···	···	3	3	···
NGC0925	9.12	-11.10±0.70	3.323±0.269	0.201±0.066	0.83±0.034	7.82±0.041	21.08±0.087	7;9	7;9	101
NGC1097	17.1	-10.95[a]	5.134±0.160	0.69±0.41	7.30±0.041	53.35±0.038	104.79±0.122	3	4	101
NGC1482	23.2	-11.80±0.05	5.682±0.202	0.692±0.010	4.68±0.044	33.36±0.060	46.73±0.068	3	3	101
NGC1512	11.8	-11.66±0.10	4.082±0.329	0.34±0.20	0.24±0.024	3.14±0.157	11.00±0.550	3	4	103
NGC1566	20.4	-10.88±0.08	4.744±1.121	0.623±0.057	3.02±0.020	22.53±0.026	58.05±0.120	3;10	10	101
NGC1705	5.1	-11.50±0.02	2.86±0.034	0.088±0.004	···	···	···	3	3	···
NGC2403	3.13	-10.25±0.04	3.418±0.271	0.217±0.045	6.29±0.944	51.55±7.733	148.49±22.274	5;7;24;25	5;6;7;24;25	102
HoII	3.39	-11.27±0.04	2.86±0.202[c]	0.12±0.07	···	···	···	assume	4	···
DDO053	3.56	-12.43±0.12	2.995±0.064	0.023±0.007	···	···	···	1	1	···
NGC2798	26.2	-11.84±0.06	4.764±0.132	0.36±0.08	3.21±0.031	20.60±0.048	29.69±0.156	3	2	101
NGC2841	14.1	-11.64±0.22	2.86±0.212	0.612±0.083	0.83±0.125	4.41±0.662	24.21±3.632	3;12	6	102
NGC2915	3.78	-11.95±0.05	2.86±0.086	0.145±0.009	···	···	···	3	3	···
HoI	3.84	-12.44±0.05	2.86±0.645	0.075±0.077	···	···	···	15	15	···
NGC2976	3.56	-11.19±0.06	3.409±0.086	0.357±0.008	1.71±0.020	13.09±0.029	33.43±0.344	3	3	101
NGC3049	23.9	-11.93±0.07	3.914±0.189	0.404±0.014	0.43±0.055	2.82±0.169	4.24±0.297	1	1	103
NGC3031	3.55	-10.32±0.05	3.033±0.368	0.545±0.084	5.42±0.813	44.73±6.710	174.02±26.103	11	6;11;19	101;102
HoIX	3.7	-13.07±0.14	2.86±0.202[c]	0.04±0.02	···	···	···	assume	4	···
M81DwB	5.3	-12.86±0.05	2.916±0.174	0.05±0.03	···	···	···	3	4	···
NGC3190	26.38	-12.68±0.05	2.86±0.392	1.532±0.197	0.35±0.084	3.19±0.351	10.11±0.506	3	3	103
NGC3184	11.1	-11.12±0.05	3.664±0.247	0.523±0.052	1.32±0.025	8.72±0.029	28.58±0.118	3;5;7	5;7	101
NGC3198	13.68	-11.40±0.04	3.447±0.160	0.304±0.018	1.08±0.029	7.15±0.041	18.44±0.103	1	1	101
IC2574	4.02	-11.23±0.07	3.722±0.141	0.046±0.017	0.08±0.012	2.41±0.362	10.62±1.593	15	15	102
NGC3265	23.2	-12.28±0.07	4.466±0.133	0.532±0.010	0.36±0.055	2.18±0.174	3.39±0.204	1	1	103
Mrk33	22.9	-11.70±0.01	3.596±0.020	0.270±0.002	0.95±0.057	4.68±0.281	5.32±0.319	1;3	1;3	103
NGC3351	9.33	-11.24±0.08	3.802±0.251	0.655±0.027	2.79±0.053	19.66±0.062	41.10±0.102	3;5;12	1	101
NGC3521	10.1	-10.85±0.04	4.769±0.109	0.558±0.008	5.46±0.082	49.19±0.100	121.76±0.405	1	1	101
NGC3621	6.55	-10.55±0.04	3.970±0.460	0.402±0.071	4.44±0.048	29.32±0.044	77.34±0.144	3;9	9	101
NGC3627	9.38	-10.74±0.05	4.611±0.350	0.55±0.05	8.55±0.071	66.31±0.059	136.56±0.118	3;22	4;22	101
NGC3773	11.9	-11.99±0.07	3.273±0.041	0.233±0.004	···	···	···	1	1	···

Table 1—Continued

Name	Distance (Mpc)	log(Hα+[NII]) (erg s^{-1} cm^{-2})	Hα/Hβ	[NII]/Hα	S$_\nu$(25 μm) (Jy)	S$_\nu$(60 μm) (Jy)	S$_\nu$(100 μm) (Jy)	references (Hα/Hβ)	references ([NII]/Hα)	references (IRAS)
(1)	(2)	(3)	(4)	(5)	(6)	(7)	(8)	(9)	(10)	(11)
NGC3938	13.4	-11.25±0.00	3.978±0.876	0.42±0.25	1.23±0.020	9.18±0.029	27.50±0.077	3	4	101
NGC4254	16.5	-10.89±0.04	4.526±0.058	0.449±0.004	4.38±0.045	37.46±0.080	91.86±0.149	1	1	101
NGC4321	14.32	-11.06±0.07	5.105±1.265	0.430±0.015	3.10±0.053	26.00±0.050	68.37±0.101	1;3	1	101
NGC4450	16.5	-12.21±0.04	3.757±0.502	0.51±0.31	···	···	···	3	4	···
NGC4536	14.45	-11.38±0.03	3.927±0.190	0.454±0.092	4.04±0.060	30.26±0.042	44.51±0.141	22;23	22	101
NGC4559	10.3	-10.97±0.05	3.528±0.232	0.281±0.148	1.03±0.030	10.23±0.044	25.41±0.074	3;9	9	101
NGC4569	16.5	-11.53±0.22	5.042±0.498	0.992±0.056	2.06±0.070	9.80±0.065	26.56±0.173	3;23	1	101
NGC4579	16.5	-11.48±0.01	3.211±0.217	0.62±0.37	0.78±0.047	5.93±0.054	21.39±0.243	3	4	101
NGC4625	9.2	-12.03±0.06	3.537±0.116	0.525±0.014	0.19±0.040	1.20±0.132	3.58±0.250	1	1	103
NGC4631	7.62	-10.55±0.06	3.711±0.063	0.28±0.06	8.97±0.046	85.40±0.062	160.08±0.260	3	2	101
NGC4736	5.20	-10.72±0.06	3.576±0.046	0.711±0.006	6.11±0.040	71.54±0.085	120.69±0.199	1	1	101
DDO154	4.3	-12.76±0.05	2.86±0.217	0.05±0.03	···	···	···	13;14	4	···
NGC4826	7.48	-11.15±0.11	3.578±0.166	0.72±0.02	2.86±0.059	36.70±0.077	81.65±0.099	3	3	101
DDO165	4.57	-12.91±0.10	2.86±0.202[c]	0.08±0.05	···	···	···	assume	4	···
NGC5033	14.8	-11.23±0.09	5.095±0.218	0.48±0.29	2.14±0.033	16.20±0.073	50.23±0.092	3	4	101
NGC5055	7.8	-10.80±0.07	4.849±1.132	0.486±0.019	6.36±0.050	40.00±0.049	139.82±0.356	5	5	101
NGC5194	8.40	-10.45±0.04	4.310±0.064	0.590±0.006	9.56±0.077	97.42±0.193	221.21±0.329	1	1	101
Tol89	16.7	-11.79[b]	3.065±0.106	0.26±0.16	0.27±0.035	1.56±0.078	2.70±0.270	3;21	4	103
NGC5408	4.81	-11.33±0.02	3.381±0.591	0.056±0.030	0.44±0.011	2.83±0.141	2.96±0.325	16;21	16;21	103
NGC5474	6.8	-11.65±0.03	2.86±0.095	0.22±0.13	0.08±0.017	1.33±0.067	4.80±0.240	3	4	103
NGC5713	29.4	-11.63±0.00	4.085±0.054	0.550±0.005	2.84±0.038	22.10±0.065	37.28±0.088	3	3	101
NGC6822	0.460	-10.54±0.04	3.252±0.228	0.048±0.032	2.46±0.369	47.63±7.140	95.42±14.300	17;18	17;18	102
NGC6946	6.8	-10.42±0.06	3.415±0.407	0.448±0.087	20.70±0.029	129.78±0.071	290.69±0.458	5;8	5;8	101
NGC7331	14.52	-11.07±0.03	3.671±1.064	0.610±0.039	5.92±0.036	45.00±0.091	110.16±0.468	12	6	101
NGC7793	3.91	-10.60±0.08	3.723±0.233	0.310±0.072	1.67±0.048	18.14±0.048	54.07±0.089	3;5;20	5;20	101

[a]No error was given in the original paper.

[b]This value is from Kennicutt et al. 2009 (in preparation). No error was given.

[c]They are low metallicity galaxies. The Hα/Hβ ratio is assumed to be 2.86 so that the estimated extinction is zero under the Case B assumption made in this paper. The error is the median error of the remaining galaxies.

References. — (1)MK06; (2)Kennicutt 1992; (3)Moustakas et al. 2008; (4)[NII]/Hα–M$_B$ relation from Kennicutt et al. (2008) (5) McCall et al. 1985; (6) Bresolin et

al. 1999; (7) van Zee et al. 1998; (8) Ferguson et al. 1998; (9) Zaritsky et al. 1994; (10) Hawley & Phillips 1980; (11) Garnett & Shields 1987; (12) Oey & Kennicutt 1993; (13) van Zee et al. 1997; (14) Kennicutt & Skillman 2001; (15) Miller & Hodge 1996; (16) Stasinska et al. 1986; (17) Peimbert et al. 2005; (18) Lee et al. 2006; (19) Stauffer & Bothun 1984; (20) Webster & Smith 1983; (21) Terlevich et al. 1991; (22) Kennicutt (unpublished); (23) this work; (24) Garnett et al. 1997; (25) Garnett et al. 1999; (101)Sanders et al. 2003; (102) Rice et al. 1989; (103) Moshir et al. 1990

Table 2. Integrated Measurements of MK06 Sample

Name	Distance	Hα	Hβ	S_ν(25 μm)	S_ν(60 μm)	S_ν(100 μm)	$S_{1.4GHz}$	references
	(Mpc)	(10^{-15} erg s^{-1} cm^{-2})	(10^{-15} erg s^{-1} cm^{-2})	(Jy)	(Jy)	(Jy)	(mJy)	(IRAS)
(1)	(2)	(3)	(4)	(5)	(6)	(7)	(8)	(9)
ARP256	113.9	1099.0±5.4	254.48±3.21	1.20±0.055	7.48±0.048	9.66±0.138	···	101
NGC0095	74.9	884.1±7.3	214.79±4.73	0.19±0.053	2.20±0.154	5.28±0.476	36.7±2.0	103
NGC0157	24.0	4311.4±24.4	1014.76±15.10	2.17±0.042	17.93±0.048	42.43±0.103	171.0[a]	101
NGC0245	56.5	1262.9±9.0	296.42±5.59	0.56±0.090	4.22±0.295	8.68±0.521	38.2±1.9	103
IC0051	24.8	1470.1±8.5	358.08±5.52	0.20±0.046	2.21±0.133	4.69±0.328	25.3±1.5	103
NGC0278	12.1	6362.0±17.1	1579.58±10.59	2.65±0.021	25.03±0.040	44.46±0.418	138.0[a]	101
NGC0337	23.5	3800.6±17.3	1096.79±12.22	0.76±0.050	9.07±0.043	20.11±0.387	106.5±3.9	101
IC1623	84.1	2764.6±5.8	666.57±2.79	3.65±0.050	22.93±0.062	31.55±0.113	248.5±9.8	101
MCG-03-04-014	139.9	490.0±3.4	86.62±1.48	0.90±0.036	7.25±0.060	10.33±0.136	43.8±1.4	101
NGC0695	135.4	1002.5±4.1	183.09±2.01	0.83±0.041	7.59±0.031	13.56±0.167	74.8±3.1	101

Note. — Table 2 is published in its entirety in the electronic edition of the Astrophysical Journal.

[a]Radio fluxes are obtained from Condon (1987). No uncertainties of the fluxes was given in that paper.

References. — (101)Sanders et al. 2003; (102) Soifer et al. 1989; (103) Moshir et al. 1990

Table 3. Measurements of Centers of SINGS Galaxies

Name	Hα[a]	Hβ[a]	[OII][a]	S$_\nu$(3.6 μm) (Jy)	S$_\nu$(8 μm) (Jy)	S$_\nu$(24 μm) (Jy)
(1)	(2)	(3)	(4)	(5)	(6)	(7)
NGC0024	91.5±2.7	31.15±2.15	74.1±6.7	0.0127±0.0013	0.0194±0.0019	0.0167±0.0007
NGC0337	552.6±4.3	153.60±2.94	318.5±8.2	0.0198±0.0020	0.0858±0.0086	0.1567±0.0063
NGC0628	69.0±2.8	18.37±2.03	10.1±4.2	0.0382±0.0038	0.0461±0.0046	0.0433±0.0017
NGC0855	379.3±3.3	114.83±2.32	292.5±6.7	0.0179±0.0018	0.0325±0.0033	0.0618±0.0025
NGC0925	281.8±3.1	84.67±2.19	184.6±6.1	0.0122±0.0012	0.0365±0.0037	0.0355±0.0014
NGC1097	2626.5±17.8	514.28±10.15	357.2±18.0	0.2725±0.0272	1.1612±0.1161	3.2867±0.1315
NGC1482	726.8±4.6	104.88±2.30	107.1±5.9	0.1559±0.0156	1.3957±0.1396	3.3599±0.1344
NGC1512	423.1±5.4	108.28±4.16	98.4±9.4	0.0703±0.0070	0.1163±0.0116	0.1496±0.0060
NGC1705	816.7±4.7	282.53±3.88	538.7±11.0	0.0121±0.0012	0.0084±0.0009	0.0219±0.0009
NGC2403	92.5±2.9	34.05±2.50	52.8±5.5	0.0267±0.0027	0.0415±0.0041	0.0403±0.0016
DDO053	110.6±1.7	39.30±1.25	88.5±4.5	0.0006±0.0001	0.0017±0.0002	0.0177±0.0007
NGC2798	1031.4±5.5	191.72±2.87	205.6±6.1	0.0826±0.0083	0.5908±0.0591	2.4276±0.0971
NGC2915	743.7±6.5	282.68±7.10	736.1±27.1	0.0128±0.0013	0.0092±0.0009	0.0285±0.0011
NGC2976	235.6±2.8	76.16±2.08	147.0±5.8	0.0175±0.0018	0.0431±0.0043	0.0886±0.0036
NGC3049	648.0±4.0	171.30±2.44	220.5±6.6	0.0129±0.0013	0.0817±0.0082	0.3646±0.0146
M81DwB	74.4±2.1	24.73±1.48	57.7±5.5	0.0011±0.0001	0.0007±0.0001	0.0026±0.0001
NGC3184	159.1±2.5	37.38±1.78	31.0±4.7	0.0215±0.0022	0.0514±0.0051	0.1181±0.0047
IC2574	82.4±2.3	26.61±1.78	69.4±6.1	0.0011±0.0001	0.0012±0.0002	0.0022±0.0001
NGC3265	341.1±3.1	79.58±1.98	114.1±5.0	0.0208±0.0021	0.0935±0.0093	0.2726±0.0109
Mrk33	1545.6±6.3	445.26±3.49	989.0±9.8	0.0197±0.0020	0.1190±0.0119	0.8359±0.0334
NGC3351	1810.3±7.7	441.89±5.39	219.5±12.4	0.1507±0.0151	0.4430±0.0443	1.5081±0.0603
NGC3773	782.7±3.9	250.70±2.44	560.3±7.1	0.0110±0.0011	0.0393±0.0039	0.1271±0.0051
NGC3938	104.0±3.0	27.86±2.34	10.6±5.7	0.0308±0.0031	0.0471±0.0047	0.0495±0.0020
NGC4254	427.7±4.6	87.60±3.22	45.8±6.0	0.0786±0.0079	0.2545±0.0255	0.3373±0.0135
NGC4321	996.3±7.9	213.21±5.30	126.2±11.8	0.1015±0.0102	0.4269±0.0427	0.7201±0.0288
NGC4536	1004.8±5.7	147.05±2.87	176.6±6.4	0.1399±0.0140	0.9692±0.0969	2.6835±0.1073
NGC4559	180.9±3.0	48.86±2.16	83.1±5.8	0.0217±0.0022	0.0582±0.0058	0.0627±0.0025
NGC4625	155.1±2.3	43.47±1.66	58.6±4.7	0.0127±0.0013	0.0399±0.0040	0.0393±0.0016
NGC4631	236.4±3.2	54.89±1.99	157.2±5.5	0.1039±0.0104	0.5595±0.0560	1.0009±0.0400
Tol89	1013.0±5.2	318.30±3.45	657.3±13.2	0.0051±0.0005	0.0044±0.0004	0.0055±0.0002
NGC5713	629.2±3.4	138.70±2.18	159.7±5.6	0.0596±0.0060	0.4412±0.0441	1.2356±0.0494
NGC6946	887.4±8.7	109.12±5.73	29.8±15.5	0.1779±0.0178	1.5100±0.1510	4.8580±0.1943
NGC7793	343.7±4.6	98.16±4.26	140.8±10.6	0.0219±0.0022	0.0614±0.0061	0.0715±0.0029

Table 3—Continued

Name	Hα[a]	Hβ[a]	[OII][a]	S_ν(3.6 μm) (Jy)	S_ν(8 μm) (Jy)	S_ν(24 μm) (Jy)
(1)	(2)	(3)	(4)	(5)	(6)	(7)

[a]The fluxes of Hα, Hβ and [OII] are in units of 10^{-15} ergs s^{-1} cm^{-2}.

Table 4. Summary of Coefficients

	adopted			dispersion		
Relation	SINGS	MK06	SINGS+MK06	SINGS	MK06	SINGS+MK06
$L(H\alpha)_{obs}$ + a*L(24 μm)	0.015±0.004	0.021±0.005	0.020±0.005	0.140	0.108	0.119
$L(H\alpha)_{obs}$ + a*L(TIR)	0.0020±0.0005	0.0025±0.0006	0.0024±0.0006	0.131	0.067	0.089
$L(H\alpha)_{obs}$ + a*L(8 μm)	0.010±0.003	···	0.011[b] ±0.003	0.112	···	0.109
$L(H\alpha)_{obs}$ + a*$L_{1.4GHz}$	0.41±0.13	0.39±0.10	0.39±0.10	0.146	0.087	0.099
$L([OII])_{obs}$ + a*L(24 μm)	···	0.029±0.005	···	···	0.136	···
$L([OII])_{obs}$ + a*L(TIR)	···	0.0036±0.0006	···	···	0.089	···
$L([OII])_{obs}$ + a*L(8 μm)	0.016[c]	···	···	0.159	···	···
$L([OII])_{obs}$ + a*$L_{1.4GHz}$	···	0.54±0.10	···	···	0.122	···

[b]This coefficient is derived based on the 20"X20" centers and the entire galaxies of SINGS sample.

[c]Because the number of data points with both [OII] and 8μm flux measurements is small, this coefficient was not derived by fitting to the data. Instead it was obtained from the combinations of Hα and 24 μm, Hα and 8 μm and [OII] and 24 μm.